European Electricity Grids May Exhibit Heatwave-induced Capacity Bottlenecks

Enming Liang[1], Minghua Chen[1,2*], Srinivasan Keshav[3*]

[1]Department of Data Science, City University of Hong Kong.
[2]School of Data Science, The Chinese University of Hong Kong (Shenzhen).
[3]Department of Computer Science and Technology, University of Cambridge.

*Corresponding author(s). E-mail(s): minghua.chen@cityu.edu.hk; sk818@cam.ac.uk;
Contributing authors: eliang4-c@my.cityu.edu.hk;

Supplementary Information

This Supplementary Information provides detailed methodological settings, extended results, and comprehensive validation studies that substantiate the main findings presented in the manuscript.

Contents

1 Detailed Data Source

We summarize the real-world publicly available datasets used in our study in Table 1, encompassing the European transmission grid, historical and future projected weather data, power demand profiles, and renewable generation models.

Supplementary Table 1 | Summary of data sources.

Data	Description
PGLIB	IEEE Testing Grid files
PyPSA-Eur [1]	Open-source dataset and configurations of European transmission network
ERA5 [2]	1940 to present hourly global climate data from ECMWF reanalysis
C3S [3]	2005 to 2100 reference climate data from C3S Energy operational service
ENTSO-E [4]	Historical hourly country-level power demand data
Demand.ninja [5]	Weather-dependent energy demand models
Atlite [6]	Open-source model for renewable generation calculation

2 Detailed Problem Formulations

We present three detailed OPF formulations featured in the main manuscript: the basic AC-OPF, the Security-Constrained (SC)-OPF, and our Temperature-Dependent (TD)-OPF model. We also discuss their simplifications and combinations used in the case studies.

2.1 Alternating Current (AC)-OPF

We consider the standard AC-OPF model [7] as the baseline in our case study:

$$\min \quad \sum_{i\in\mathcal{N}} \sum_{k\in\mathcal{G}_i} c_{i,k} \cdot P_{i,k}, \tag{1}$$

s.t.

$$\text{Power flow balance} \quad \begin{cases} \sum_{k\in\mathcal{G}_i} P_{i,k} - P_i^d = \mathrm{re}\left(V_i(\sum_{j\in\mathcal{N}} Y_{ij}V_j)^*\right) \\ \sum_{k\in\mathcal{G}_i} Q_{i,k} - Q_i^d = \mathrm{im}\left(V_i(\sum_{j\in\mathcal{N}} Y_{ij}V_j)^*\right) \end{cases}, \ \forall i \in \mathcal{N}, \tag{2}$$

$$\text{Line flow limits} \quad |V_i\left((V_i - V_j)\, Y_{ij}\right)^*| \le S_{ij}^{\max}, \ \forall (i,j) \in \mathcal{L}, \tag{3}$$

$$\text{Generations limits} \quad P_{i,k} \in [P_{i,k}^{\min}, P_{i,k}^{\max}], Q_{i,k} \in [Q_{i,k}^{\min}, Q_{i,k}^{\max}], \ \forall i \in \mathcal{N}, \ \forall k \in \mathcal{G}_i, \tag{4}$$

$$\text{Voltage limits} \quad |V_i| \in [V_m^{\min}, V_m^{\max}], \ |\angle V_{ij}| \le V_a^{\max}, \ \forall i \in \mathcal{N}, \ \forall (i,j) \in \mathcal{L}, \tag{5}$$

$$\text{var.} \quad \boldsymbol{P}, \boldsymbol{Q}, \text{ and } \boldsymbol{V}.$$

The detailed descriptions are presented in Table 2.

Compared to commonly adopted linear/DC-OPF models (e.g., in PyPSA [1]), AC-OPF models can capture transmission line thermal losses and resistance variations, which are essential for conductor thermal modeling in temperature-dependent analysis.

Supplementary Table 2 | Parameters of the power grid model.

Notation	Description
$\mathcal{T}$	set of time slots
$\mathcal{N}$	set of buses
$\mathcal{L}$	set of lines
$\mathcal{C}$	set of contingency of line outage
$\mathcal{G}_i,\ \forall i \in \mathcal{N}$	set of generators at each bus
$\mathcal{S}_l,\ \forall l \in \mathcal{L}$	set of segments at each line
$V_i,\ \forall i \in \mathcal{N}$	complex voltage at each bus
$P_i^d, Q_i^d,\ \forall i \in \mathcal{N}$	active and reactive power demand at each bus
$P_{i,k}, Q_{i,k},\ \forall i \in \mathcal{N},\ \forall k \in \mathcal{N}_i$	active and reactive power generation for each generator
$c_{i,k},\ \forall i \in \mathcal{N},\ \forall k \in \mathcal{N}_i$	generation cost for each generator
$P_l, Q_l, I_l,\ \forall l = (i,j) \in \mathcal{L}$	active, reactive power flow and current at each line
$T_{l,s},\ \forall l \in \mathcal{L},\ \forall s \in \mathcal{S}_l$	temperature for each segment at each line
$d_{l,s},\ \forall l \in \mathcal{L},\ \forall s \in \mathcal{S}_l$	length for each segment at each line
$Y_l, G_l, B_l, R_l, X_l,\ \forall l \in \mathcal{L}$	admittance, conductance, susceptance, resistance, reactance

We also note that AC-OPF is commonly used in single-snapshot formulations [8], as multi-period AC-OPF becomes computationally expensive due to non-linear constraints. Conversely, linear/DC-OPF models are typically used in multi-period formulations for long-term planning, where temporal trade-offs are more important than detailed power-flow accuracy [9].

2.2 Security Constrained (SC)-OPF

Security constraints are important operational requirements for power grids, where N-1 security requirements are commonly modeled [10]. This ensures that the power system can still operate within safe ranges under any single transmission line outage. Let $\mathcal{C}$ be the set of possible line outages that would not induce network disconnectivity. The standard SC-OPF is formulated as:

$$\begin{aligned}
&\min && (1) && (6)\\
&\text{s.t.} && && (6)\\
&\text{Base constraints} && (2)-(5), && (6)\\
&\text{Post. PF balance} && \begin{cases} \sum_{k\in\mathcal{G}_i} P_{i,k}^c - P_i^d = \mathrm{re}\left(V_i(\sum_{j\in\mathcal{N}} Y_{ij}^c V_j^c)^*\right) \\ \sum_{k\in\mathcal{G}_i} Q_{i,k}^c - Q_i^d = \mathrm{im}\left(V_i(\sum_{j\in\mathcal{N}} Y_{ij}^c V_j^c)^*\right) \end{cases}, \forall i \in \mathcal{N},\ c \in \mathcal{C} && (7)\\
&\text{Post. line flow limits} && |V_i^c \left(\left(V_i^c - V_j^c\right) Y_{ij}^c\right)^*| \le S_{ij}^{\max},\ \forall (i,j) \in \mathcal{L},\ c \in \mathcal{C} && (8)\\
&\text{Post. Gen. limits} && P_{i,k}^c \in [P_{i,k}^{\min}, P_{i,k}^{\max}], Q_{i,k}^c \in [Q_{i,k}^{\min}, Q_{i,k}^{\max}],\ \forall i \in \mathcal{N},\ \forall k \in \mathcal{G}_i,\ c \in \mathcal{C} && (9)\\
&\text{Post. Vol. limits} && |V_i^c| \in [V_m^{\min}, V_m^{\max}],\ |\angle V_{ij}^c| \le V_a^{\max},\ \forall i \in \mathcal{N},\ \forall (i,j) \in \mathcal{L},\ c \in \mathcal{C} && (10)\\
&\text{Ramping limits:} && \|\boldsymbol{P} - \boldsymbol{P}^c\|_\infty \le \Delta_p, \|\boldsymbol{Q} - \boldsymbol{Q}^c\|_\infty \le \Delta_q, \|\boldsymbol{V} - \boldsymbol{V}^c\|_\infty \le \Delta_v, \forall c \in \mathcal{C} && (11)\\
&\text{Base-case var.} && \boldsymbol{P}, \boldsymbol{Q},\ \text{and}\ \boldsymbol{V}, \qquad \text{Post-case. var.} \quad \boldsymbol{P}^c, \boldsymbol{Q}^c,\ \text{and}\ \boldsymbol{V}^c, \forall c \in \mathcal{C}
\end{aligned}$$

Security constraints ensure the post-contingency constraints from (7) to (11). The base case and post-contingency case are coupled with the ramping constraints. For preventive settings, the real power generation is fixed as $\Delta_p = 0$, and for corrective settings, all decision variables are adjustable within prescribed ranges.

Since the number of decision variables and constraints grows linearly with the number of contingencies, existing works focus on simplifying scenario constraints, such as a fixed percentage reduction (e.g., 70%) of thermal limits in ACOPF model provides a safety margin [11]; and a linearized security constraint based on Branch-Outage-Distribution-Factor (BODF) models contingency impacts in the linearized DCOPF model [12].

We conduct standard AC-based N-1 preventive security constraints in IEEE 30 experiments under heatwaves, as it provides exact topology and system configuration, and is computationally feasible. We then use the commonly adopted 70% fixed security margin in the large-scale European countries analysis [1] due to (i) inexact topology due to clustering and (ii) computational burden.

2.3 Temperature Dependent (TD)-OPF

Standard AC-OPF neither incorporates the impact of weather on the electrical network's parameters, such as resistance, nor considers the dynamic thermal limits of transmission lines. TD-OPF [13–15] with transmission line thermal modeling is formulated as:

$$
\begin{aligned}
&\text{min} && (1) && \\
&\text{s.t.} && && \\
&\text{ACOPF constraints} && (2)-(5), && \\
&\text{Heat balance equations} && T_{l,s} = \mathcal{H}(I_l, \mathcal{W}_{l,s}),\ \forall s \in \mathcal{S}_l && (12)\\
&\text{Conductor thermal limits} && T_{l,s} \le T^{\max},\ \forall s \in \mathcal{S}_l && (13)\\
&\text{Line resistance} && R_l = \sum_{s \in \mathcal{S}_l} d_{l,s} \cdot R(T_{l,s}) && (14)\\
&\text{Line current flow} && I_l = |(V_i - V_j) Y_{ij}|,\ \forall l = (i,j) \in \mathcal{L}, && (15)\\
&\text{Line admittance} && Y_l = 1/(R_l + \mathrm{i} \cdot X_l),\ \forall l = (i,j) \in \mathcal{L}, && (16)\\
&\text{var.} && \boldsymbol{P}, \boldsymbol{Q}, \text{ and } \boldsymbol{V}. &&
\end{aligned}
$$

Besides the regular AC-OPF constraints, TD-OPF models incorporate the thermal behavior and thermal limits under specific weather conditions. It models the steady-state line temperature, which involves non-linear equations and is constrained by the maximum allowable temperature (e.g., 90℃). The line temperature also determines the line resistance and changes the power grid admittance, which in turn impacts the OPF modeling. The coupling between power flow and heat flow via line current makes solving the exact TD-OPF computationally expensive.

Existing studies focus on simplifying the thermal modeling via linear or quadratic approximations. In dynamic line rating (DLR) related studies [16–19], only the thermal

limits are considered, which are transformed into branch flow limits as

$$I_l \leq I_l^{\max} = \mathcal{H}^{-1}(T^{\max}, W_{l,s}) \tag{17}$$

and equivalently reformulated into line power flow constraints by multiplying the per-unit voltage. Such DLRs are typically used in linear OPF models without dynamic coupling between power flow and heat flow.

On the other hand, the thermal behavior is approximated by a quadratic curve due to the Joule heating effects, such that thermal limits can be simplified as:

$$\beta_0(W_{l,s}) + \beta_1(W_{l,s})I_l^2 + \beta_2(W_{l,s})I_l^4 \leq T^{\max} \tag{18}$$

where the coefficients depend on the specific line weather conditions $W_{l,s}$ [20].

3 EU Simulation Settings

3.1 Setting Overview

Supplementary Table 3 | Notable European Heatwave Records (in 2019 and 2022)

Country	Year	Temperature	Location
Spain	2019	44.4°C	Albuquerque, Badajoz
	2022	45.8°C	Torremocha del Campo
Portugal	2019	43.1°C	Alvega, Santarem
	2022	47.0°C	Pinhão
France	2019	46.0°C	Vérargues
	2022	42.6°C	Biscarrosse
Italy	2019	40.8°C	Rome
	2022	46.6°C	Perugia
Germany	2019	42.6°C	Lingen
	2022	40.3°C	Bad Mergentheim
UK	2019	38.7°C	Cambridge
	2022	40.3°C	RAF Coningsby
Belgium	2019	41.8°C	Begijnendijk
	2022	40.0°C	Kapelle-op-den-Bos
Netherlands	2019	40.7°C	Gilze-Rijen
	2022	39.5°C	Maastricht-Aachen Airport

[1] References: [2019 European heatwaves]; [2022 European heatwaves].
[2] Temperatures represent the highest recorded during each respective heatwave period

To assess the resilience of the European electricity grid under projected future heatwave conditions, we employ an integrated modeling approach that combines the data sources detailed in Table 1 (main manuscript) with the computational framework described in Section 2 (main manuscript). Our analysis focuses on Western

Supplementary Table 4 | Installed Capacity by Country and Technology Type

Country	Conv.[a] (GW)	Renew.[b] (GW)	Stor.[c] (GW)
Spain	39.99	67.89	23.79
Portugal	4.50	8.73	5.08
France	64.17	37.96	13.67
Italy	47.62	32.55	11.77
Germany	72.37	117.59	7.24
UK	49.91	51.54	0.66
Belgium	10.79	9.88	1.18
Netherlands	17.57	21.87	0.00

[a] Conv. = Conventional (fossil fuel and nuclear power plants)
[b] Renew. = Renewable (wind, solar, hydro, and biomass power plants)
[c] Stor. = Storage units (battery and H2 storage units)
Note: Installed capacity remains constant across all resolution levels.

European countries that have historically experienced significant heatwave events, as documented in Supplementary Table 3.

We derive country-specific power grid representations using PyPSA-Eur [1, 11]. Our methodology begins by extracting the complete EU grid profile and subsequently filtering for the regions of interest. To address potential local modeling inaccuracies—including misalignment of load and supply distributions and inadequate representation of urban underground transmission infrastructure—we adopt a clustered grid network approach supported by the PyPSA framework. This clustering methodology consolidates proximate buses and transmission lines, thereby simplifying the grid representation while minimizing error-induced transmission bottlenecks [1, 21].

The approach first distributes the target number of clusters across countries proportionally to their electrical loads by solving an assignment problem that minimizes the deviation between integer cluster assignments and the ideal proportional allocation. It then applies weighted k-means clustering within each country separately, incorporating regional electrical load as weights to ensure that high-demand regions receive adequate representation in the simplified network topology.

To balance computational efficiency with network fidelity, we adopt a 75% resolution clustered network relative to the initial 380 kV transmission network configuration. We apply k-means clustering [21] to aggregate buses into larger geographical areas, preserving essential power flow patterns while reducing computational complexity. This clustering addresses fundamental modeling artifacts in ENTSO-E-derived network topologies [1]. These models exhibit unrealistic load shedding even with sufficient generation capacity, stemming from two key issues: (1) Voronoi cell assignments that inaccurately map loads and generators to substations, failing to represent actual distribution grid topology; and (2) underrepresentation of inner-city underground cabling. The 75% resolution effectively smooths these local assignment errors while maintaining network characteristics critical for our analysis. Country-specific power grid configurations and operational parameters are detailed in Tables 4 and 5.

To incorporate weather-induced thermal limits, it is essential to model the physical properties and operational requirements of transmission lines. In our case study, we standardize transmission lines to the "Al/St 240/40 4-bundle 380.0" specification,

Supplementary Table 5 | Power Grid Configuration at Different Resolutions

Country	Buses	Lines	Number of Generator/Storage		
			Conv.[a]	Renew.[b]	Stor.[c]
Spain	281	442	91	339	75
Portugal	81	129	14	66	24
France	439	711	53	652	51
Italy	373	522	93	622	65
Germany	484	682	792	936	31
UK	319	426	90	451	6
Belgium	42	50	23	82	3
Netherlands	34	41	30	64	0

[a] Conv. = Conventional (fossil fuel and nuclear power plants)
[b] Renew. = Renewable (wind, solar, hydro, and biomass power plants)
[c] Stor. = Storage units (battery and H2 storage units)

featuring an aluminum/steel cross-section of 240/40 mm^2 and a 4-bundle configuration of wires per phase at 380 kV [1, 22]. Conventional aluminum/steel conductors (e.g., ACSR, AAC, AAAC) typically operate within temperature ranges of 80°Cto 120°C[17, 23–25].

To address security constraints as operational requirements, we follow established methodologies [16, 26] by implementing a simplified N-1 security criterion, limiting transmission line flows to 70% of their maximum capacity. This approximation is justified by two considerations: first, the aggregated network topology does not perfectly represent real-world grid configurations; second, full security-constrained optimization with non-linear heat flow modeling becomes computationally intractable for large-scale European network models.

3.2 Heatwave Generation

We generate future European heatwave scenarios for 2026-2030 using the morphing methodology detailed in Section 2.1 of the main manuscript. These projections build upon historical extreme events—specifically the 2019 and 2022 heatwaves (Table 3)—which serve as baseline templates. Our approach combines hourly ERA5 reanalysis data (temperature, solar radiation, and wind speed) with future climate projections from the Copernicus Climate Change Service (C3S) energy sector indicators. This methodology preserves the spatial patterns and diurnal cycles of observed extremes while incorporating climate change amplification factors. Temperature and solar irradiance undergo additive bias correction in their original space, while wind speed is morphed in log-space to ensure physically positive values.

Generated weather variables for future heatwaves in Spain are presented in Figures 1 through 3. Each figure contains: **a**: Demonstrates the morphing approach for simulating future heatwaves, where delta values calculated from historical heatwave days (in July 2022) are applied to future reference hot days. **b**: Shows spatial distributions of weather variables for both historical and future reference conditions and their corresponding heatwaves. **c**: Displays the 2030 heatwave scenarios generated using delta values from the five hottest historical days, with separate visualizations for different sampled bus areas in the electricity grid.

For other countries, we provide condensed visualizations in Figures 4 through 10 to show the temperature profiles of generated heatwaves.

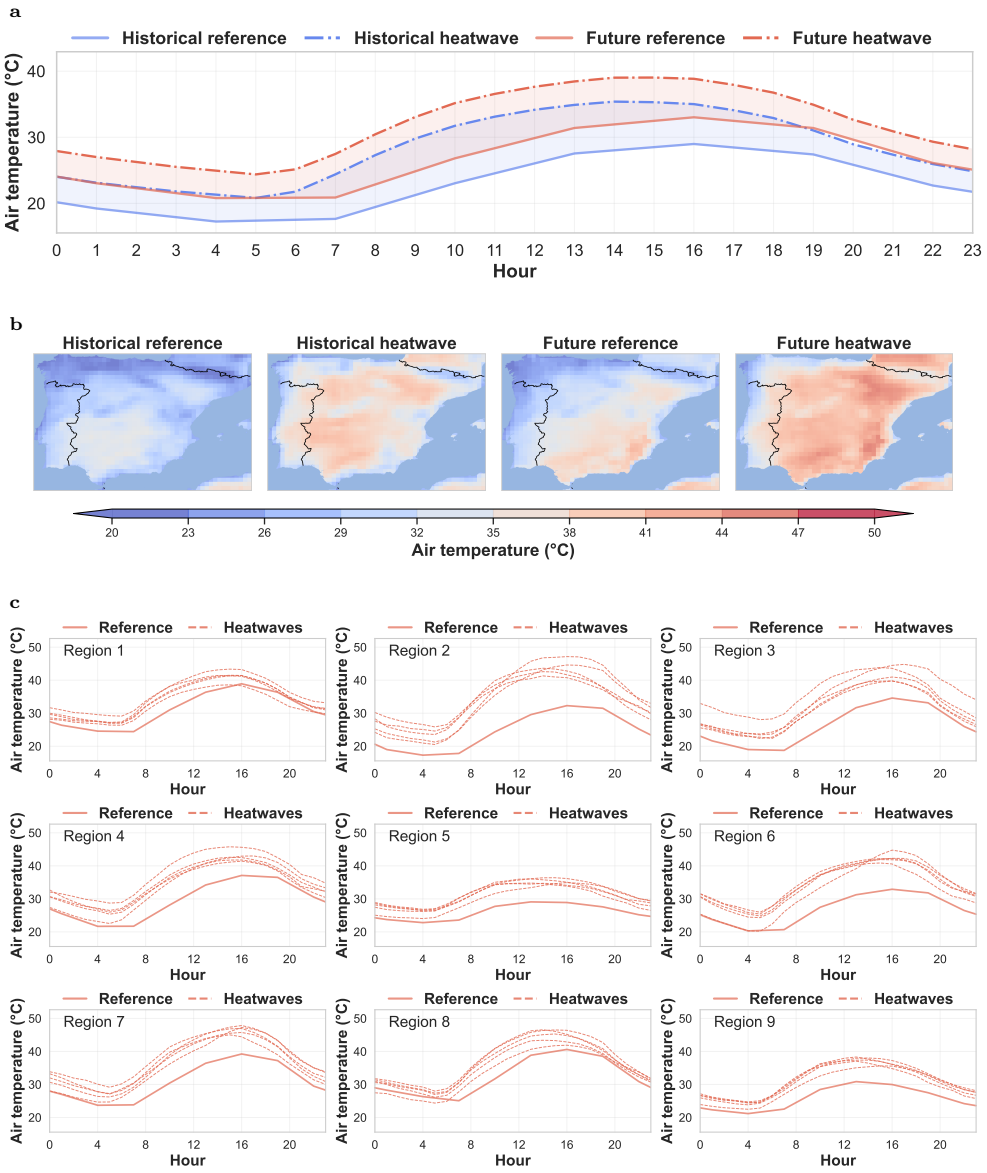

Supplementary Figure 1 | Generated temperature profiles during heatwaves in Spain by 2030 compared to the 2022 records.

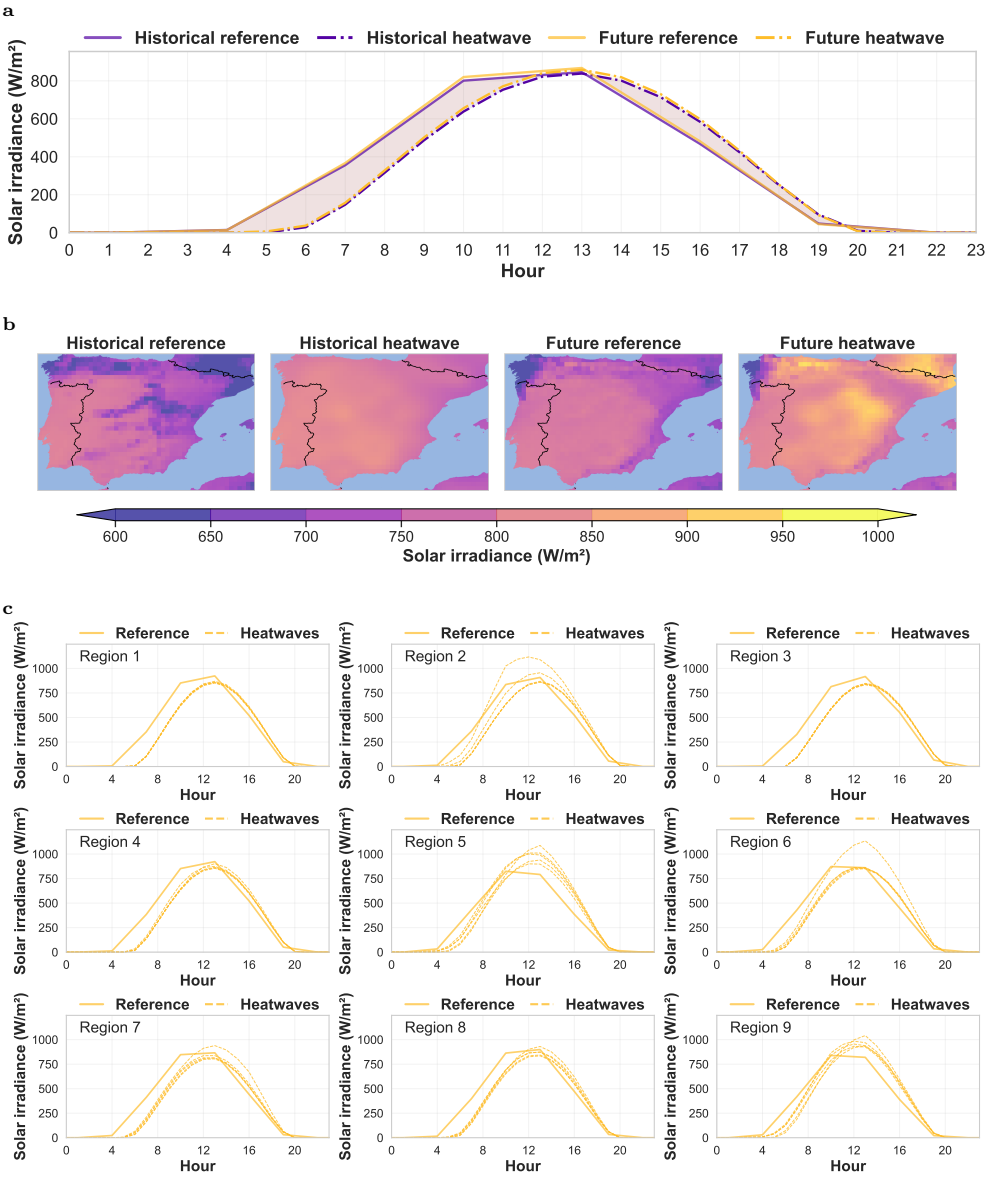

Supplementary Figure 2 | Generated solar radiation profiles during heatwaves in Spain by 2030 compared to the 2022 records.

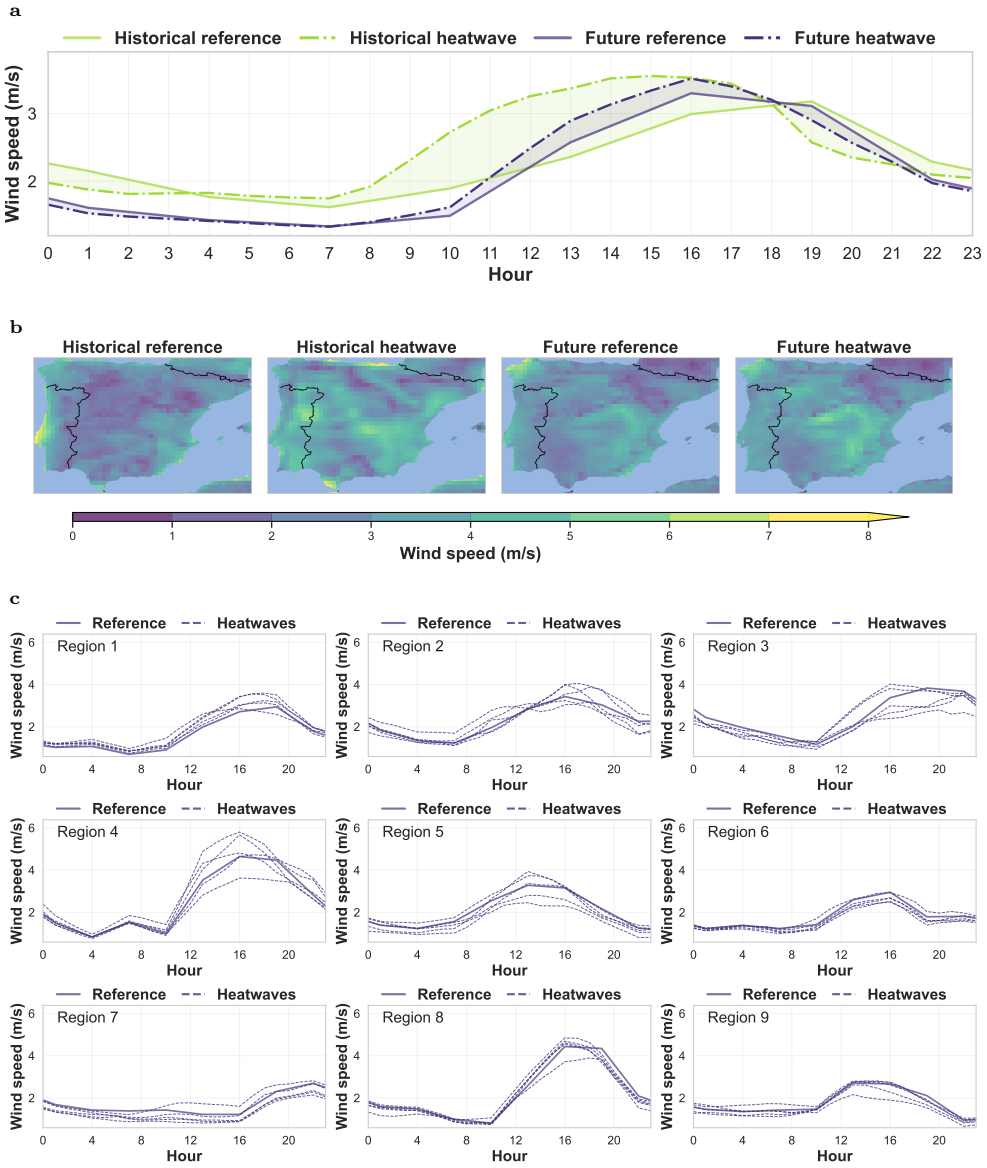

Supplementary Figure 3 | Generated wind speed profiles during heatwaves in Spain by 2030 compared to the 2022 records.

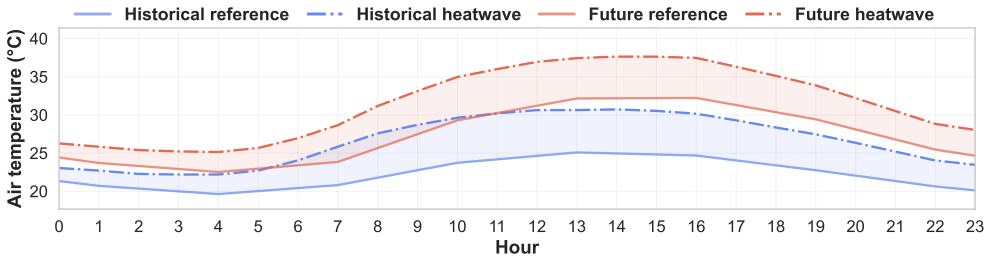

Supplementary Figure 4 | Generated temperature profiles during heatwaves in Italy by 2030 compared to the 2022 records.

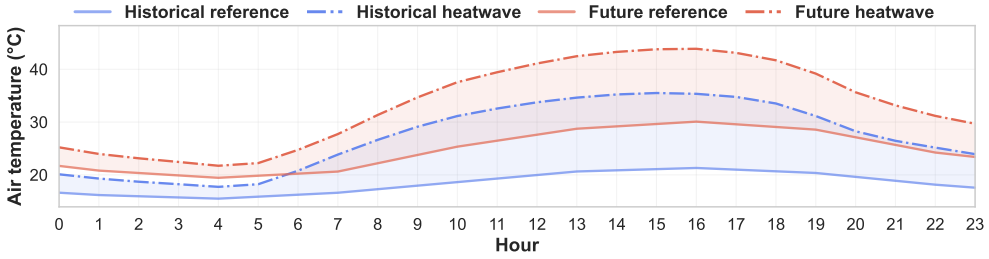

Supplementary Figure 5 | Generated temperature profiles during heatwaves in France by 2030 compared to the 2022 records.

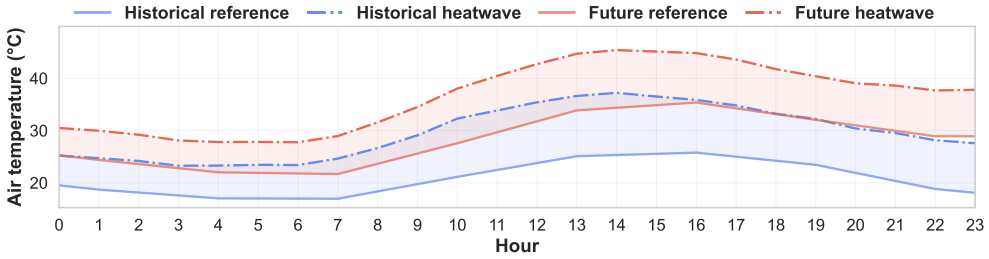

Supplementary Figure 6 | Generated temperature profiles during heatwaves in Portugal by 2030 compared to the 2022 records.

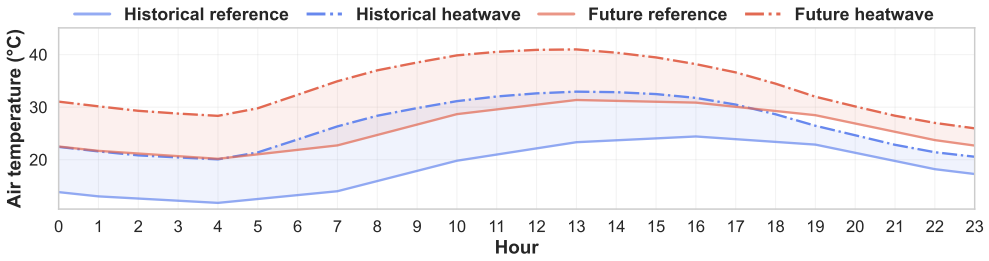

Supplementary Figure 7 | Generated temperature profiles during heatwaves in Germany by 2030 compared to the 2022 records.

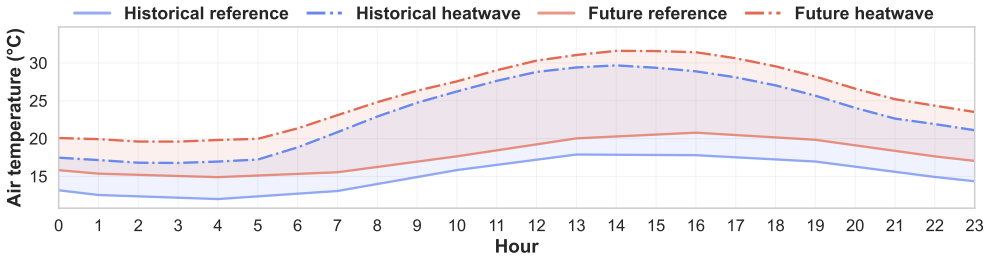

Supplementary Figure 8 | Generated temperature profiles during heatwaves in the UK by 2030 compared to the 2019 records.

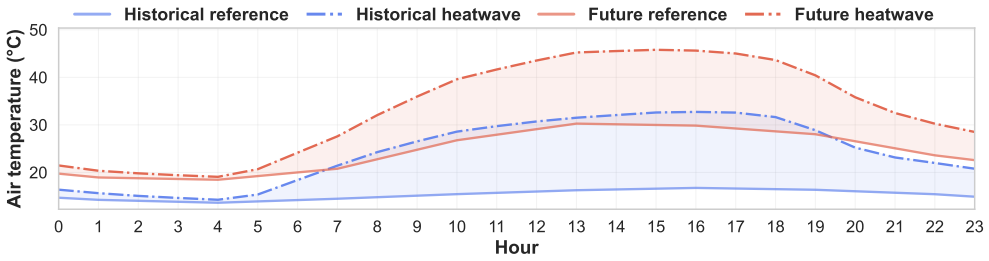

Supplementary Figure 9 | Generated temperature profiles during heatwaves in Belgium by 2030 compared to the 2022 records.

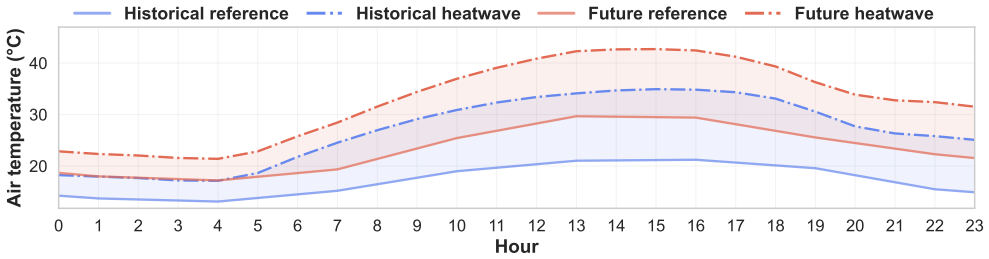

Supplementary Figure 10 | Generated temperature profiles during heatwaves in the Netherlands by 2030 compared to the 2022 records.

3.3 Demand Calibration

Supplementary Table 6 | Demand model calibration for Western European countries.

Country	P_{base} (GW)	P_{heat} (GW/℃)	P_{cool} (GW/℃)	T_{heat} (℃)	T_{cool} (℃)	α (GW)
Spain	22.32	0.60	0.79	14.93	19.16	4.45
Portugal	4.75	0.17	0.17	15.65	19.14	0.90
France	38.38	2.46	0.66	14.19	20.82	6.32
Italy	25.51	0.60	1.53	12.39	19.29	8.01
Germany	44.56	0.64	0.67	15.10	22.28	11.53
UK	30.02	1.26	0.58	15.46	17.32	5.10
Belgium	7.96	0.16	0.18	15.95	18.14	1.20
Netherland	10.71	0.17	0.15	14.87	17.76	1.66

[1] Key parameters include baseline demand (P_{base}), heating coefficient (P_{heat}), cooling coefficient (P_{cool}), heating threshold temperature (T_{heat}), cooling threshold temperature (T_{cool}), and weekday demand difference coefficient (α).
[2] Demand models are calibrated based on historical hourly load data from 2015 to 2024 for all countries except Great Britain. Great Britain is calculated based on data from 2015 to 2020, given the availability of load data on the ENTSO-E platform.

We develop temperature-dependent electricity demand models following the demand.ninja framework [5], as detailed in Section 2.2 (main manuscript). Since Demand.ninja does not provide publicly available code for model calibration and raw data processing, we implement their methodology [5] to calibrate demand models for the EU countries in our case study. We leverage historical hourly load data from ENTSO-E (from 2015 to 2024) in conjunction with historical ERA5 weather records, enabling us to capture the complex, non-linear relationships between ambient temperature and electricity consumption patterns across diverse European countries.

We employ the open-source black-box optimizer PyPop7 [27] to calibrate the demand models and derive country-specific parameters. The calibration results and model performance are presented in Figure 11. The results clearly reveal the cooling threshold temperatures and cooling load demand coefficients under hot conditions, providing a valid foundation for simulating temperature-induced demand changes under extreme heatwave scenarios.

For model calibration based on historical data from 2015 to 2024, we do not incorporate the growth rate parameter, which derives an average estimation for the baseline country demand. However, for future scenarios, we incorporate varying annual growth rates (β) to model different load projection pathways. This approach accounts for emerging grid challenges from AI technologies, smart homes, and electric vehicles, which are expected to significantly alter historical demand patterns. By adjusting these growth rates, we evaluate grid performance under various electrification scenarios, ranging from moderate to aggressive technology adoption trajectories.

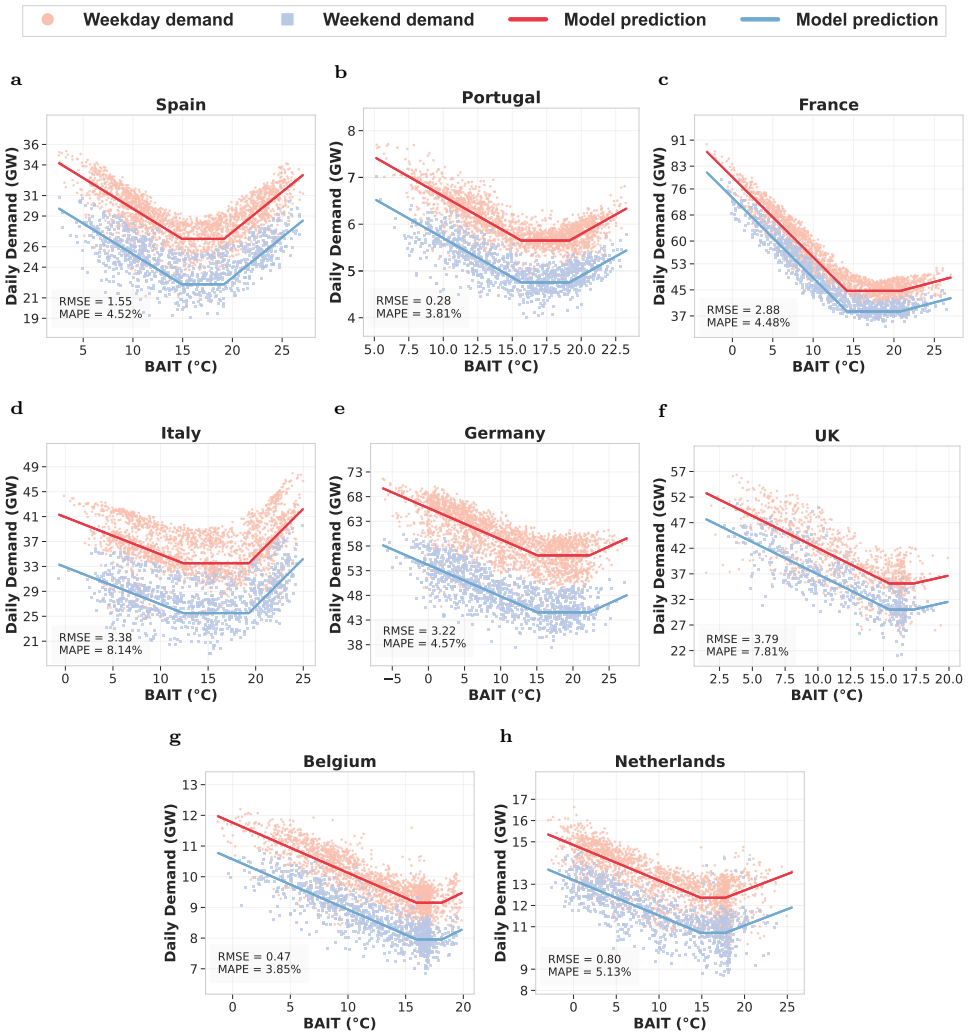

Supplementary Figure 11 | Demand calibration for Western EU countries.

3.4 Conductor Thermal Models

3.4.1 Single Conductor Heat Balance

Heatwaves also reduce transmission capacity in power grids by affecting the thermal behavior of overhead conductors. This physical phenomenon can be modeled by the steady-state heat balance equation, which accounts for the equilibrium between heat generated by electrical current and solar radiation, and heat lost through convection, radiation, and conduction. The specific steady-state heat balance equation according

to IEEE Std 738$^{\text{TM}}$-2012 [28] used in our study is as follows:

$$\underbrace{H_C + H_R}_{\text{heat loss}} = \underbrace{H_S + H_J}_{\text{heat gain}} \quad [\text{W/m}], \tag{19}$$

where

$$H_C = \max \begin{cases} 3.645\rho_f^{0.5} D^{0.75} \left(T - T_{\text{amb}}\right)^{1.25}, & \text{(zero wind speed)}; \\ K_\phi \left[1.01 + 1.35 N_{\text{Re}}^{0.52}\right] \lambda_f \left(T - T_{\text{amb}}\right), & \text{(low wind speed)}; \\ 0.754 K_\phi N_{\text{Re}}^{0.6} \lambda_f \left(T - T_{\text{amb}}\right), & \text{(high wind speed)}; \end{cases} \tag{20}$$

$$H_R = \pi \sigma_B D \alpha_{\text{emi}} \left[(T + 273)^4 - (T_{\text{amb}} + 273)^4\right] \tag{21}$$

$$H_S = \alpha_{\text{abs}} D S \tag{22}$$

$$H_J = I^2 R(T) = I^2 R_{\text{ref}}(1 + \alpha_r (T - T_{\text{ref}})) \tag{23}$$

Here, H_C is the heat loss rate due to convective cooling affected by air temperature, wind speeds, angles, and the conductor temperature; H_R is the heat loss rate due to radiative cooling caused by the temperature difference, H_S is the heat gain rate due to solar radiation and H_J is the heat gain rate due to Joule heating under conductor current and temperature-dependent resistance. The values of these coefficients are specified in Table 7.

Supplementary Table 7 | Parameters in the conductor thermal model.

Notation	Description
ϕ	The angle between wind and axis of conductor, taking value in $[0, \pi/2]$
K_ϕ	Wind direction factor, $K_\phi = 1.194 - \cos(\phi) + 0.194\cos(2\phi) + 0.368\sin(2\phi)$
V_{w}	Wind speed [m/s]
D	Conductor diameter [m]
L	Conductor length [m]
S	Total solar heat intensity [W/m^2]
N_{re}	Dimensionless Reynolds number, $N_{\text{re}} = D\rho_f V_{\text{w}}/\mu_f$
ρ_f	Density of air [kg/m^3]
μ_f	Dynamic viscosity of air
λ_f	Thermal conductivity of air [W/(m $\cdot$ °C)]
α_{emi}	Radiation emissivity factor, taking values in $[0, 1]$
α_{abs}	Solar absorptivity factor, taking values in $[0, 1]$
α_r	Temperature-dependent resistance coefficient
σ_B	Stefan–Boltzmann constant $\sigma_B = 5.67 \times 10^{-8}$ [W/(m$^2 \cdot$ K^4)]
$T, T_{\text{amb}}, T_{\text{ref}}$	Conductor, ambient, and reference temperature [$^\circ C$]
$R(T_c)$	Unit temperature-dependent resistance [Ω/m]

3.4.2 Conductor Thermal Limits

Conductor thermal limits vary substantially across different technologies, as established in the literature and industry standards (Table 8). Conventional conductors, including Aluminum Conductor Steel Reinforced (ACSR), All Aluminum Conductor (AAC), and All Aluminum Alloy Conductor (AAAC), typically operate within temperature ranges of 80℃ to 120℃ [17, 23, 29]. In contrast, modern High Temperature

Low Sag (HTLS) conductors—such as Aluminum Conductor Steel Supported (ACSS), Aluminum Conductor Carbon Composite Reinforced (ACCR), ZTACIR, and Aluminum Conductor Carbon Core (ACCC)—are designed for continuous operation at significantly higher temperatures ranging from 180℃ to 250℃ [17].

European transmission standards establish conservative operational limits for conventional conductors. According to ENTSO-E technical specifications [25], these conductors should not exceed 80℃ under worst-case ambient conditions. Contemporary European network simulations, particularly PyPSA-based models of the EU transmission system [1, 16], typically adopt a 100℃ maximum temperature limit for conventional conductors.

For this study, we selected 90℃ as the maximum thermal limit for conventional conductors, representing a middle ground between the European standard limit and common simulation practices. This choice accounts for both operational safety margins and realistic network conditions. Regarding HTLS conductors, their deployment remains limited primarily to pilot projects and small-scale field tests, such as those conducted in Northern Germany and documented by ENTSO-E [30]. Given their current limited deployment, we focus our analysis on conventional conductor limits while acknowledging the potential for future HTLS integration.

Supplementary Table 8 | Summary of conductor thermal limits in literature.

Reference	Conductor Type	Thermal Limits
[23]	Conventional	80℃–120℃
[24]	ACSR	50℃–180℃
[29]	ACSR	90℃–110℃
[17]	Traditional (ACSR, AAC, AAAC) Modern (ACSS, ACCR, ZTACIR, ACCC)	<100℃ 180℃–250℃
[25]	Conventional	80℃
[30]	HTLS	Up to 210℃
[1, 16]	Conventional (in PyPSA)	100℃

3.4.3 Multi-Bundle Heat Balance

In practice, multi-bundle transmission lines are commonly employed for long-distance power transmission, which significantly complicates thermal modeling due to mutual thermal interactions between conductors. The convective and radiative cooling of individual conductors is reduced when they are positioned in the wake of other conductors, creating complex heat transfer patterns that deviate from single-conductor assumptions. For instance, the PyPSA-Eur documentation specifies "Al/St 240/40 4-bundle 380.0" as the default conductor configuration for 380 kV transmission networks, representing a four-bundle conductor arrangement within a single transmission line. Such multi-bundle configurations are standard practice in high-voltage applications to reduce corona discharge and improve power transfer capacity.

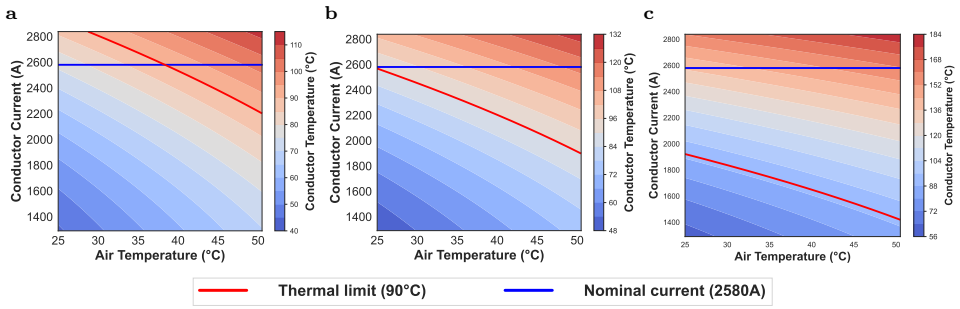

Supplementary Figure 12 | Thermal analysis of Al/St 240/40 4-bundle 380 kV conductor under worst-case ambient conditions [25]. The conductor thermal equilibrium is evaluated at 0.6 m/s wind speed and 900 W/m^2 solar irradiance across varying ambient temperatures and current loads. Figures **a**, **b**, and **c** display steady-state conductor temperatures under individual, corrected, and merged conductor modeling frameworks, respectively.

Exact modeling of multi-conductor thermal behavior requires sophisticated finite-element simulations [31], which showed that steady-state temperatures of individual conductors within a bundle can vary by 5-25°C due to mutual thermal influences. This temperature variation has important implications for ampacity calculations and thermal limit assessments.

Given the computational complexity of exact modeling, two primary approaches are typically employed to simplify multi-conductor thermal analysis:

- **Individual Conductor Modeling (Fig. 13 (a))**: One simplification approach neglects the mutual thermal influence among conductors and treats each bundle as an independent line [1], which is implemented in the dynamic line rating functionality of PyPSA. This simplification **overestimates** the transmission line capacity by failing to account for the reduced convective and radiative cooling effects that occur in multi-bundle configurations, where conductors shield each other from airflow and thermal radiation.
- **Merged Conductor Modeling (Fig. 13 (c))**: An alternative simplification merges multiple bundles into a single equivalent transmission line, which neglects the physical spacing between individual conductors within the bundle. This single-line modeling approach is predominantly adopted in existing temperature-dependent optimal power flow (OPF) formulations [14, 32]. The method assumes uniform heat distribution and cooling across the entire conductor cross-section, which **underestimates** the transmission capacity due to convective cooling between the physical space of individual bundles.

Corrected Conductor Modeling (Fig. 13 (b)): To account for mutual thermal effects while maintaining computational efficiency in multi-bundle conductor modeling, we introduce a corrective factor applied to the cooling components H_C (convective cooling) and H_R (radiative cooling). Drawing from finite-element analysis results

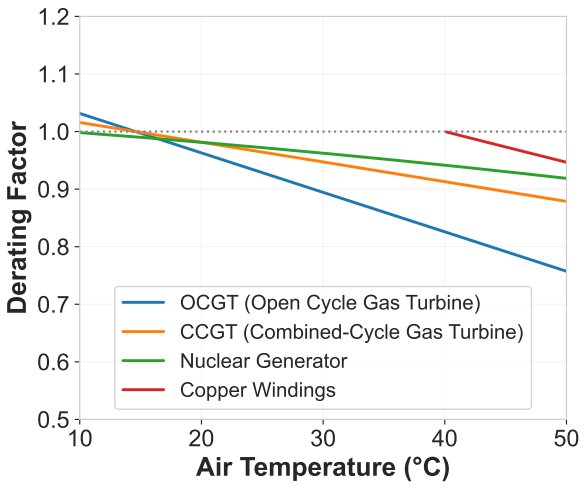

Supplementary Figure 13 | Generator derating factor under different temperatures. The capacity derating factor (η) for various generator types as a function of ambient temperature, showing how generating capacity diminishes during high-temperature events. This thermal sensitivity becomes particularly significant during heatwaves when multiple generators experience simultaneous capacity reductions.

---

reported in [31], which demonstrated that steady-state temperatures of individual conductors within a bundle can vary by 5-25℃ depending on their physical position due to mutual thermal interactions, we adopt a correction factor of 0.8. The modified heat balance equation becomes: $0.8 \cdot H_C + 0.8 \cdot H_R = H_S + H_J$. Under worst-case ambient conditions as defined by ENTSO-E [25]—0.6 m/s wind speed, 900 W/m^2 solar irradiance, and maximum current flow—our model predicts that conductors reach the 90℃ thermal limit at an ambient temperature of approximately 25℃. This corrected capacity curve falls between the individual conductor and merged bundle modeling approaches. Specifically, our results show approximately 15℃ difference compared to the individual conductor (optimistic setting) modeling approach, which aligns well with the empirical finite-element analysis findings reported in [31].

3.5 Generator Derating Effects

As discussed in the main manuscript, generators experience derating with increasing temperatures during heatwaves, with the magnitude varying across different generator types and weather conditions. We quantify these thermal dependencies through a capacity derating factor $\eta \leq 1$ for conventional generators operating under elevated ambient temperatures ($T_{\text{amb}} \geq 20°C$), as illustrated in Figure 13.

4 EU Simulation Results

4.1 Setup

Based on generated future weather profiles (2026-2030) derived from the 2019 and 2022 European heatwaves, we transform renewable generation profiles according to the corresponding weather inputs. We analyze a total of 480 heatwave scenarios per country, comprising **5 years × 24 daily heatwave projections × 4 hottest hourly snapshots = 480 scenarios**. Specifically, we select the historically hottest days in June and July in 2019, 2022, and 2024 as heatwave events, then apply the bias-correction methods described in Sec. 3.2 to create future heatwave projections. Load profiles are projected using our calibrated demand model with a baseline annual growth rate of 1% from 2025. For single-snapshot analyses, we set the state of charge (SoC) for storage units to 80% as an optimistic setting. Using these parameters, we conduct optimal power flow analysis and model comparison for selected countries. Table 9 provides the detailed model configurations used for comparisons throughout our main manuscript and supplementary information.

Metrics. To evaluate extreme heatwave impacts on national power grids, we employ three key metrics: (1) **load shedding ratio**, representing unserved load as a percentage of total hourly demand; (2) **line temperature**, calculated via the heat balance equation using current flows from OPF solutions; and (3) **capacity reduction**, computed by as the ratio of thermal-induced line transmission capacity relative to nominal ratings. These metrics collectively quantify grid vulnerability and operational constraints during extreme heat events.

We then conduct a **single-country analysis** via OPF for each selected country under projected heatwaves in Sec. 4.2. We also conduct **cross-border analysis** to examine grid interdependencies across multiple countries in Sec. 4.3.

4.2 Heat-flow Analysis for Single Country

We first provide a compact summary of simulation results for eight Western EU countries in Fig. 14, based on the proposed Iter-OPF framework (incorporating temperature-dependent modeling for grid analysis and solved using our iterative algorithm). This summary encompasses three key aspects: statistics of temperature and load demand under projected heatwave scenarios; load shedding magnitude and computational running time under the proposed Iter-OPF analysis; and the distribution of line temperatures and associated capacity reductions under projected heatwave conditions.

We then present detailed analyses for three countries—Spain, Italy, and France—which exhibit substantial load shedding under projected heatwaves (Figs. 15–23). For these case studies, we examine three dimensions.

▷ First, in our model comparison, we evaluate performance across countries under the generated heatwave scenarios, examining load shedding, line temperatures, and computational requirements relative to four baseline models (Figs. 15, 18, 21).

Supplementary Table 9 | Model Baselines for the EU-Grid Simulations.

Models	**Conductor model** Thermal	Segments	**Generator** Derating	**Contingency** Security Constraint
	Model Basleines			
AC-OPF	✗	✗	✗	✗
Quad-OPF	quad. approx.	✗	✗	✗
Iter-OPF	✓	✓	✓	✗
TD-OPF	✓	✓	✓	✗
	Ablation Study			
w/o thermal	✗	✓	✓	✗
w/o segment	✓	✗	✓	✗
w/o derating	✓	✓	✗	✗
SC-OPF	✗	✗	✗	70%

[1] The model baselines include existing and proposed approaches for analyzing grid performance under extreme heatwaves. AC-OPF represents a standard alternating current OPF without heat balance constraints. Quad-OPF applies a quadratic approximation for heat balance and thermal limit constraints. Iter-OPF uses the proposed iterative approach for solving the complete temperature-dependent OPF model. TD-OPF represents the fully converged solution for the exact TD-OPF model.
[2] The ablation study examines the contribution of individual model components. "w/o thermal" excludes the thermal-dynamic conductor model. "w/o segment" removes line segmentation and uses average weather along the line for thermal modeling. "w/o derating" omits generator derating factors. SC-OPF incorporates a 70% security constraint margin without thermal modeling.

▷ Second, in our temporal analysis, we investigate trends from 2025 to 2030 in load shedding and line temperatures, considering varying load growth rates and storage deployment levels to assess their impacts on network resilience (Figs. 16, 19, 22).

▷ Third, in our sensitivity analysis, we conduct ablation studies on the proposed iterative framework by systematically removing individual modeling components to quantify their contributions, benchmarking against the simplified security-constrained optimal power flow model with a 70% security margin [1]. We further quantify the impacts of the underlying physical thermal models by comparing individual-conductor modeling with corrected models that account for bundle effects, and by examining conductors with different thermal limits (Figs. 17, 20, 23).

Key observations include the following. First, existing OPF models overestimate grid resilience under heatwaves, highlighting the need for temperature-dependent formulations. Second, complete thermal modeling is essential for accurate resilience assessment under heatwaves, as simplified approaches fail to capture critical thermal constraints. Third, rising demand amplifies grid stress, yet energy storage alone offers limited relief, suggesting that infrastructure upgrades and demand-side management must complement storage deployment. Fourth, grid vulnerability differs substantially by country, reflecting variations in network topology, generation mix, and climatic exposure.

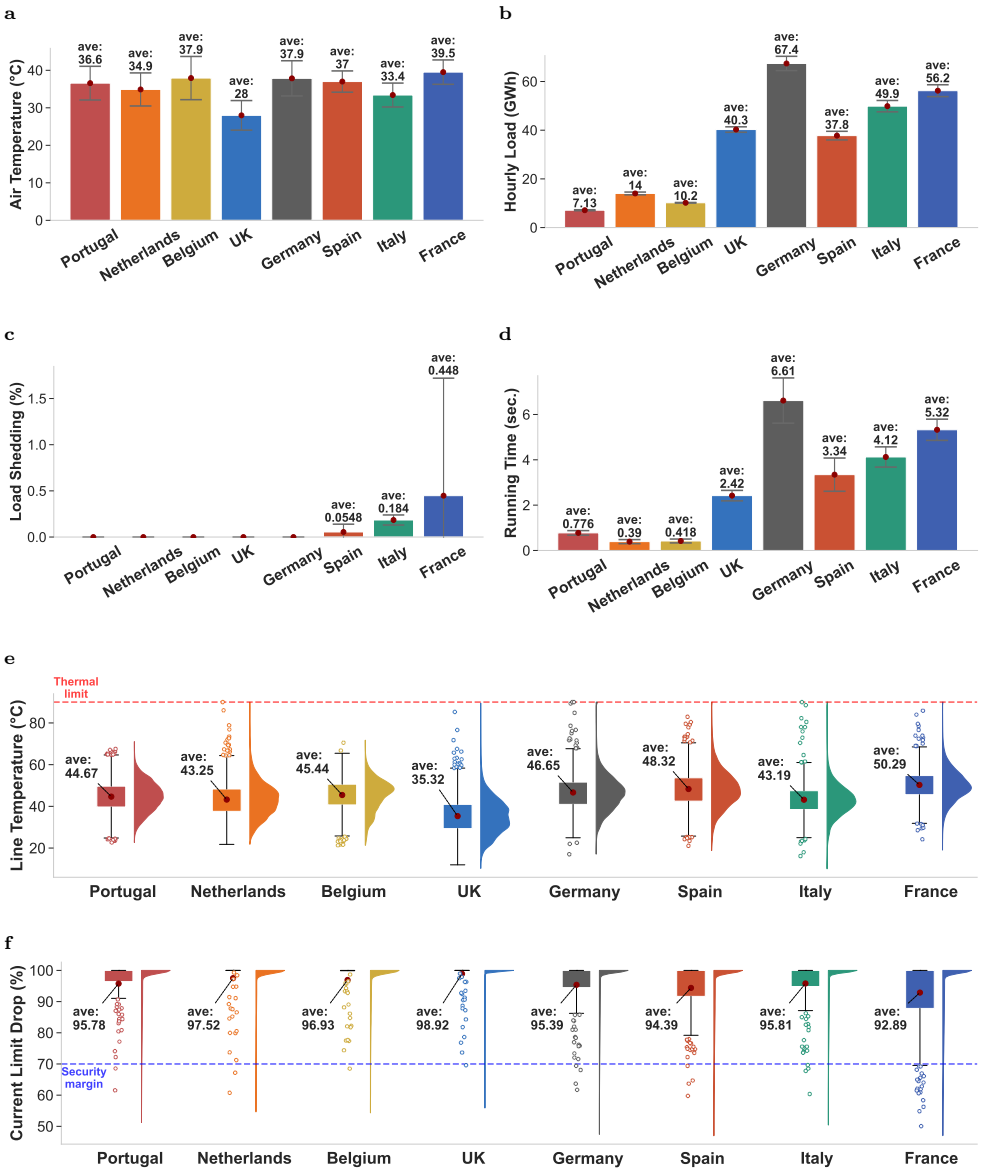

Supplementary Figure 14 | National grids in Western Europe, such as France, Italy, and Spain, exhibit substantial load shedding under projected heatwaves, while other countries remain resilient. a Average air temperature during the hottest hours in projected heatwave periods. **b** Average hourly load demand for heatwave scenarios estimated by calibrated demand models. **c** Average load shedding across different countries. **d** Average running time per scenario for different national grids. **e** Distribution of line temperature under OPF analysis with projected heatwaves. **f** Distribution of line capacity reduction compared to nominal ratings during heatwaves.

4.2.1 Spain

a

Year	Wind (m/s)	Solar (W/m^2)	Temp. (℃)	Load (GWh)
2026	2.27 (±0.37)	785.52 (±67.23)	36.05 (±2.59)	36.47 (±1.45)
2027	2.87 (±0.36)	753.82 (±70.45)	36.92 (±2.58)	37.48 (±1.33)
2028	2.65 (±0.40)	717.83 (±91.25)	36.93 (±3.46)	37.98 (±2.12)
2029	2.62 (±0.43)	789.08 (±66.75)	37.52 (±2.58)	38.23 (±1.36)
2030	2.69 (±0.35)	766.68 (±62.69)	37.58 (±2.58)	38.71 (±1.62)

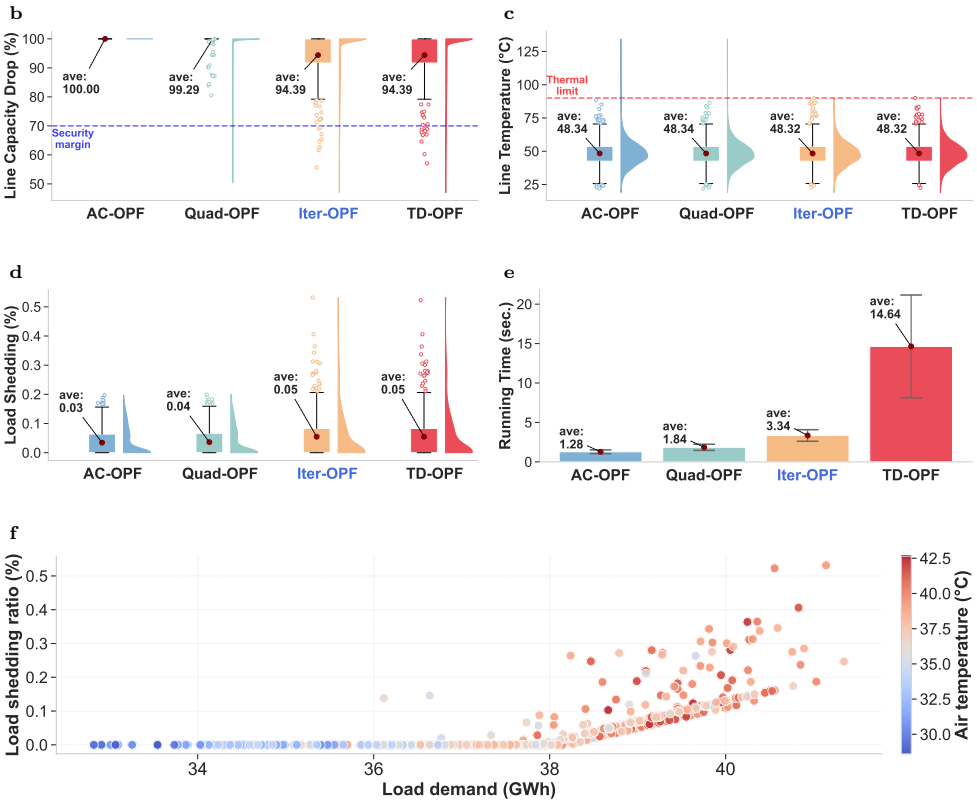

Supplementary Figure 15 | OPF analysis comparison in Spanish Grid. a Weather and load statistics under heatwave projections from 2026 to 2030, with 480 scenarios generated using a bias-correction approach. **b-c** Distributions of estimated line capacity reduction compared to nominal conditions and line temperatures (derived from heat balance equations). Box plots display the median (centre line), interquartile range (box), and 1.5× interquartile range (whiskers); violin plots show the probability density distribution. **d** Distributions of load shedding ratios (demand-generation mismatch over total demand) **e** Average per-scenario solving times. **f** Relations between air temperature, load demand, and load shedding ratio.

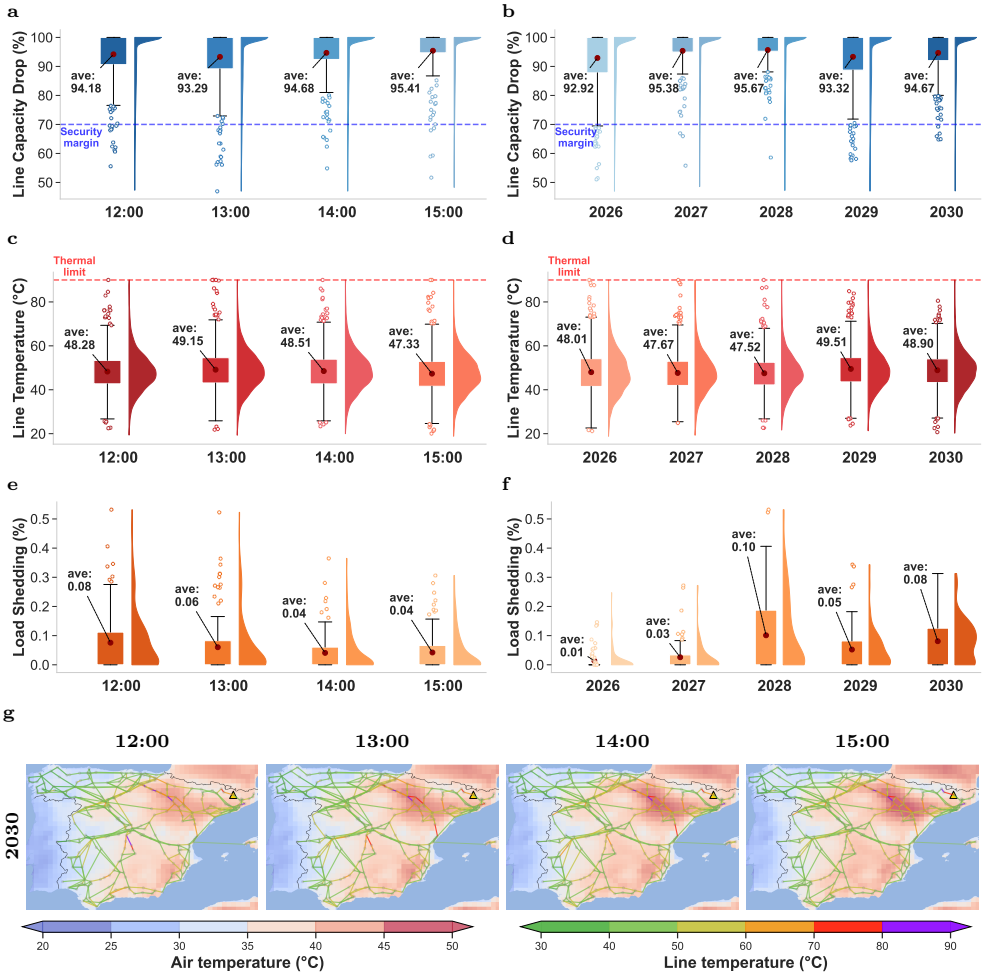

Supplementary Figure 16 | Spatiotemporal evolution of grid thermal stress and load shedding under heatwave conditions across diurnal and interannual scales. a–b Line capacity drop across different times of day (a) and projection years (b), with the security margin indicated by the dashed blue line. **c–d** Transmission line temperature variations across hours of day (c) and projection years (d); dashed red line indicates the thermal limit. **e–f** Load shedding ratios as a function of time of day (e) and projection year (f). **g** Power grid visualization showing the spatial distribution of air temperature (background shading; redder indicates higher temperature) and transmission line temperature (network overlay; red/purple indicates proximity to thermal limits) during peak afternoon hours (12:00–15:00) for a sampled heatwave scenario in 2030. Yellow triangles (△) indicate buses experiencing load shedding.

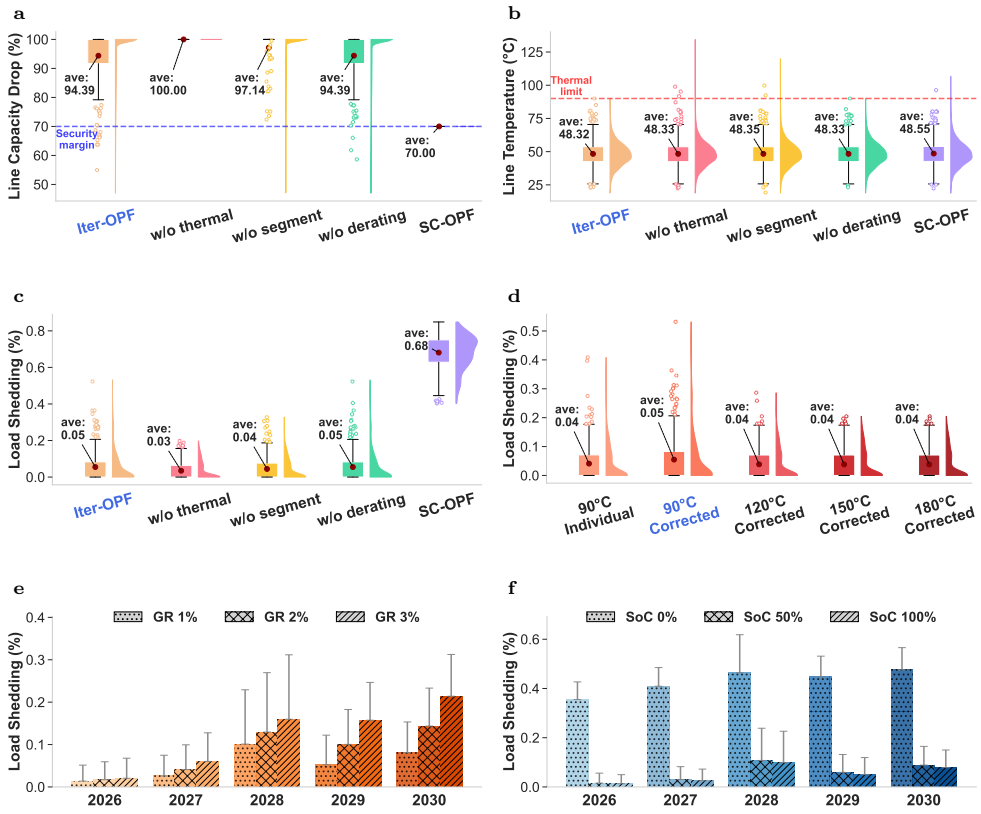

Supplementary Figure 17 | Ablation study of thermal modeling, impacts of the physical thermal model, and sensitivity to load growth and storage conditions under heatwave scenarios. **a**–**c**, Impact of removing different modeling components from the Iter-OPF framework on capacity reduction (a), line temperatures (b), and load shedding ratios (c), compared to the 70% security margin SC-OPF method. **d**, Sensitivity of load shedding to different physical thermal models (detailed in Sec. 3.5) and thermal limit assumptions (individual conductor model at 90°C versus corrected model with thermal ratings at 90°C, 120°C, 150°C, and 180°C). **e**–**f**, Sensitivity analysis of load shedding ratios under varying annual load growth rates (GR: 1%, 2%, and 3%) (e) and initial battery state-of-charge levels (SoC: 0%, 50%, and 100%) (f). Box plots display the median (centre line), interquartile range (box), and 1.5× interquartile range (whiskers); violin plots show the probability density distribution.

4.2.2 Italy

a

Year	Wind (m/s)	Solar (W/m^2)	Temp. (℃)	Load (GWh)
2026	1.95 (±0.23)	661.30 (±103.10)	31.11 (±2.62)	47.27 (±1.48)
2027	2.45 (±0.23)	603.16 (±113.85)	32.65 (±3.41)	49.22 (±2.33)
2028	1.94 (±0.26)	677.70 (±106.83)	33.93 (±2.63)	50.37 (±1.51)
2029	2.20 (±0.30)	660.80 (±120.41)	34.22 (±2.83)	50.80 (±1.92)
2030	2.07 (±0.19)	688.94 (±113.99)	35.13 (±2.76)	51.72 (±1.40)

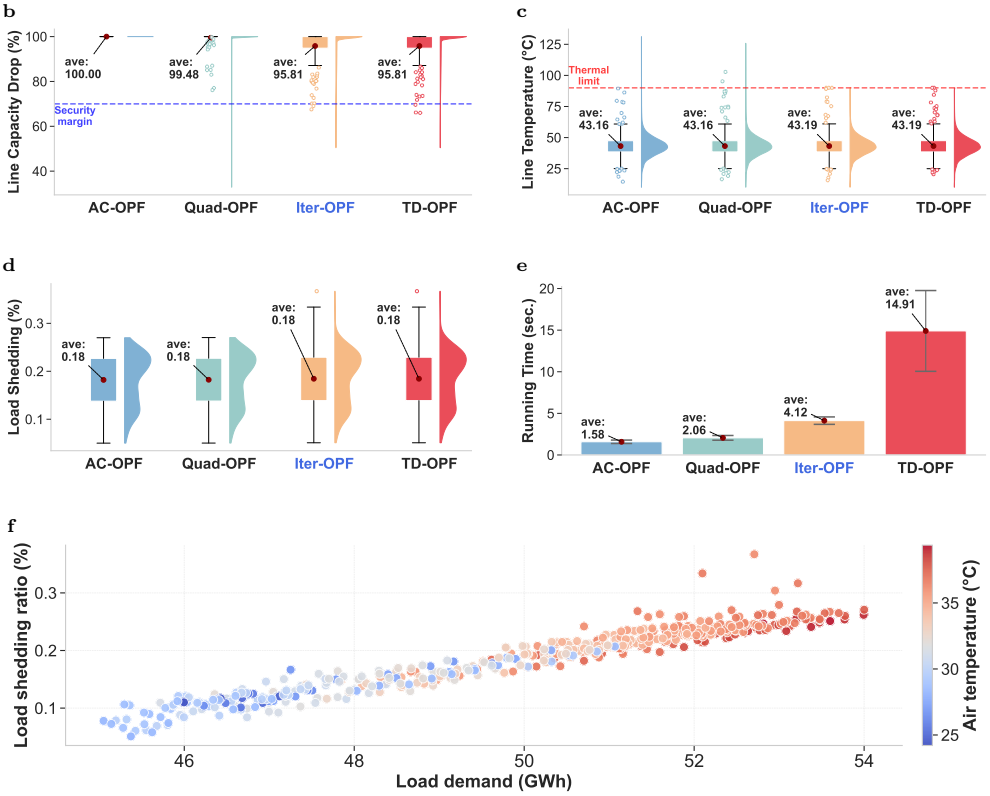

Supplementary Figure 18 | OPF analysis comparison in Italian Grid. a Weather and load statistics under heatwave projections from 2026 to 2030, with 480 scenarios generated using a bias-correction approach. **b-c** Distributions of estimated line capacity reduction compared to nominal conditions and line temperatures (derived from heat balance equations). Box plots display the median (centre line), interquartile range (box), and 1.5× interquartile range (whiskers); violin plots show the probability density distribution. **d** Distributions of load shedding ratios (demand-generation mismatch over total demand) **e** Average per-scenario solving times. **f** Relations between air temperature, load demand, and load shedding ratio.

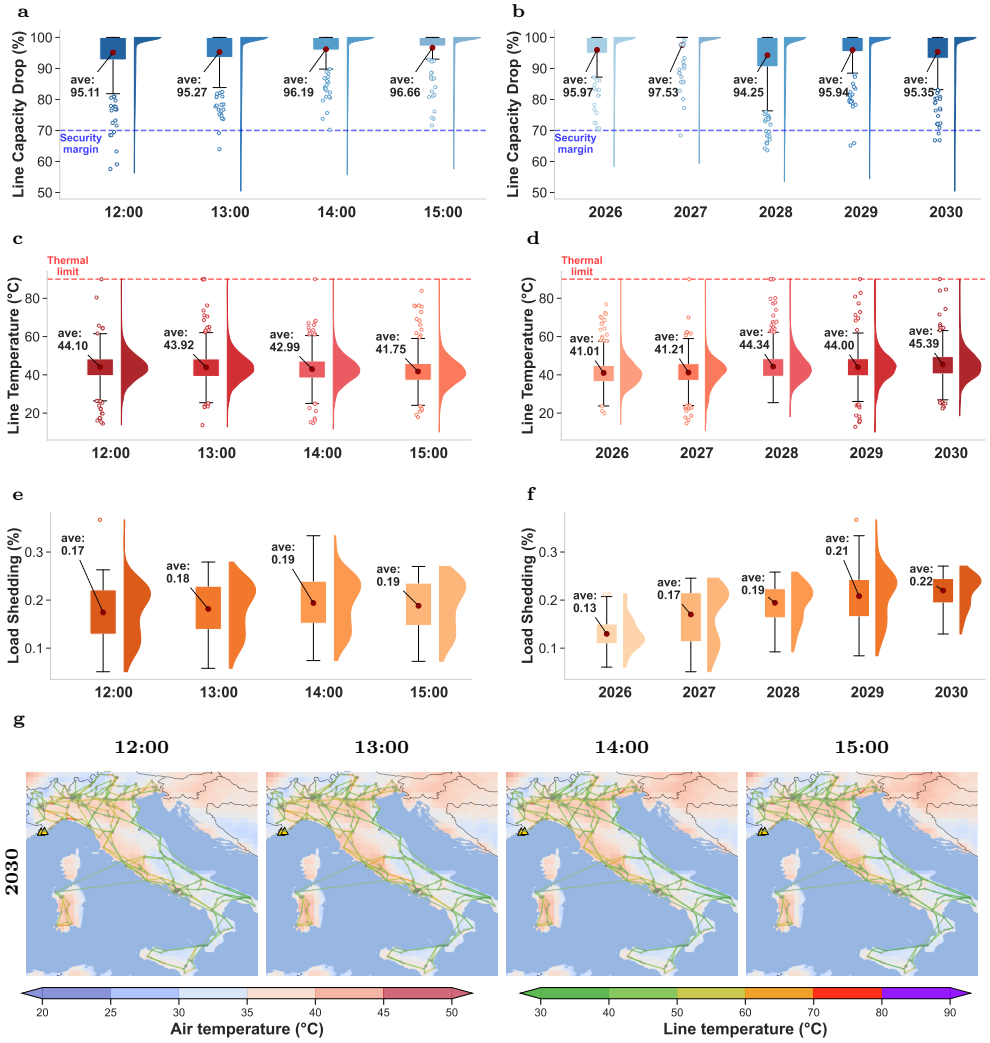

Supplementary Figure 19 | Spatiotemporal evolution of grid thermal stress and load shedding under heatwave conditions across diurnal and interannual scales. a–b Line capacity drop across different times of day (a) and projection years (b), with the security margin indicated by the dashed blue line. **c–d** Transmission line temperature variations across hours of day (c) and projection years (d); dashed red line indicates the thermal limit. **e–f** Load shedding ratios as a function of time of day (e) and projection year (f). **g** Power grid visualization showing the spatial distribution of air temperature (background shading; redder indicates higher temperature) and transmission line temperature (network overlay; red/purple indicates proximity to thermal limits) during peak afternoon hours (12:00–15:00) for a sampled heatwave scenario in 2030. Yellow triangles (△) indicate buses experiencing load shedding.

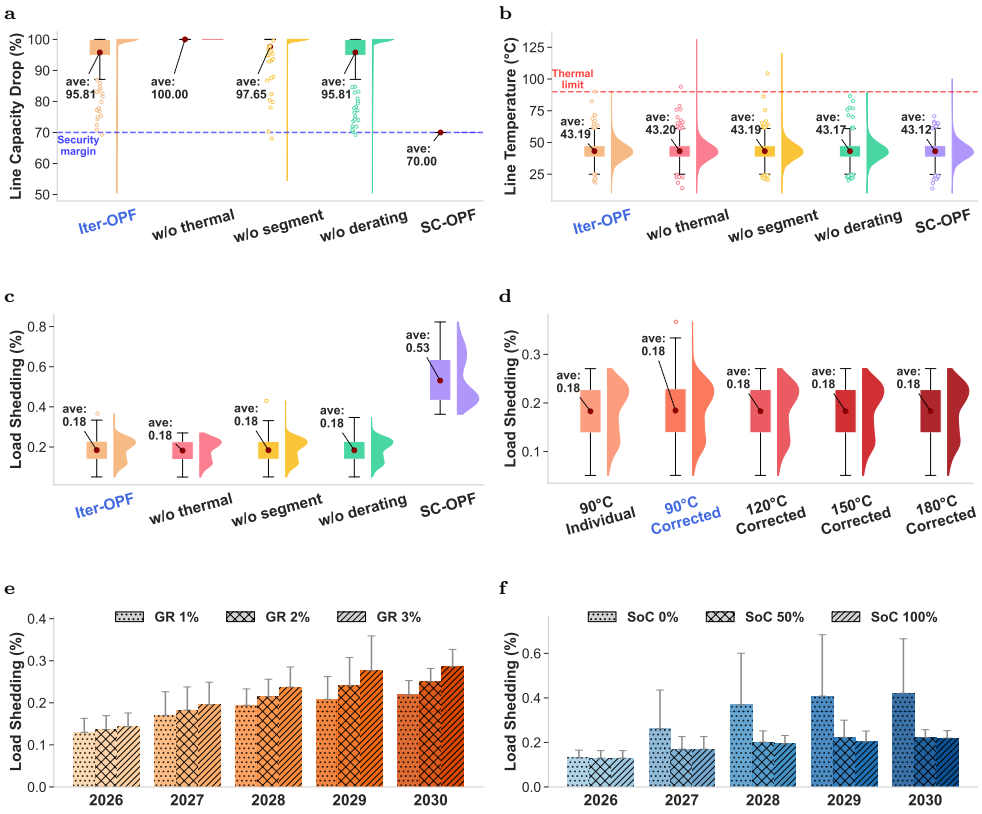

Supplementary Figure 20 | Diurnal-to-interannual evolution of grid performance and sensitivity to load growth and storage conditions under heatwave scenarios. f-h Impact of removing different modeling components from the Iter-OPF framework on capacity reduction (f), line temperatures (g), and load shedding ratios (h), compared to the 70% security margin SC-OPF method. **g–h** Sensitivity analysis of load shedding ratios under varying annual load growth rates (GR: 1%, 2%, and 3%) (g) and initial battery state-of-charge levels (SoC: 0%, 50%, and 100%) (h).

4.2.3 France

a

Year	Wind (m/s)	Solar (W/m^2)	Temp. (℃)	Load (GWh)
2026	2.32 (±0.61)	788.31 (±80.97)	37.59 (±1.67)	54.53 (±1.56)
2027	2.19 (±0.52)	753.01 (±102.57)	37.39 (±3.70)	53.92 (±1.52)
2028	1.97 (±0.33)	784.75 (±102.22)	42.43 (±2.79)	58.63 (±1.65)
2029	2.24 (±0.55)	870.64 (±68.62)	39.84 (±2.90)	56.70 (±1.97)
2030	2.55 (±0.80)	811.68 (±78.75)	40.32 (±1.66)	57.35 (±1.70)

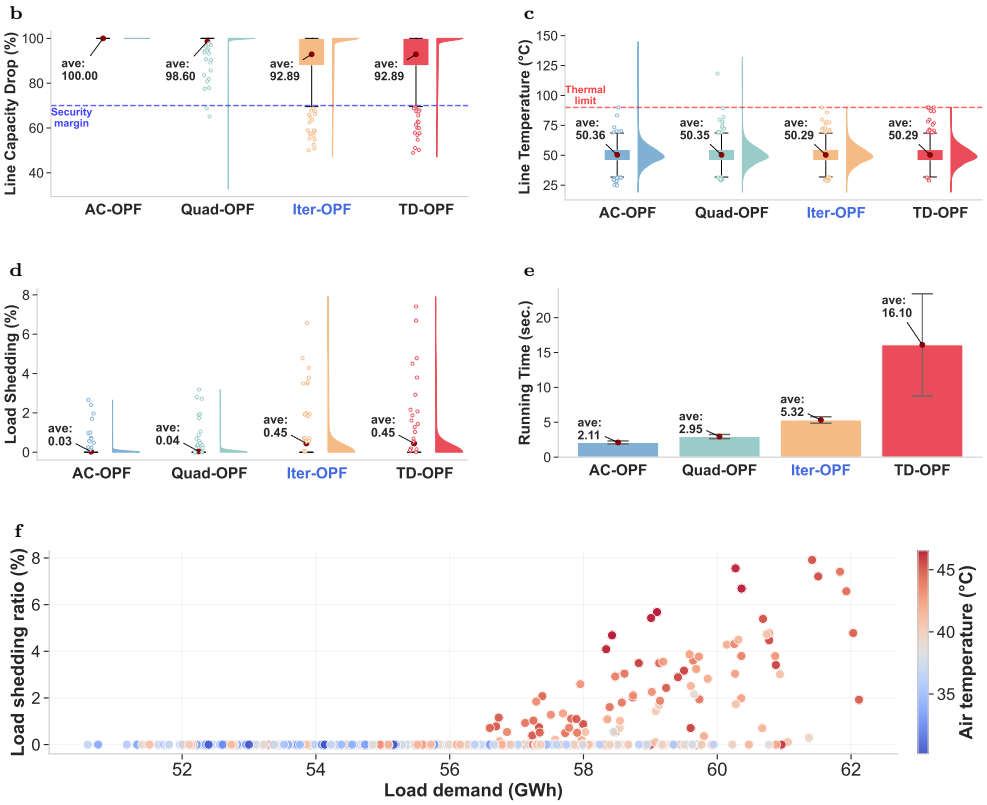

Supplementary Figure 21 | OPF analysis comparison in French Grid. a Weather and load statistics under heatwave projections from 2026 to 2030, with 480 scenarios generated using a bias-correction approach. **b-c** Distributions of estimated line capacity reduction compared to nominal conditions and line temperatures (derived from heat balance equations). Box plots display the median (centre line), interquartile range (box), and 1.5× interquartile range (whiskers); violin plots show the probability density distribution. **d** Distributions of load shedding ratios (demand-generation mismatch over total demand) **e** Average per-scenario solving times. **f** Relations between air temperature, load demand, and load shedding ratio.

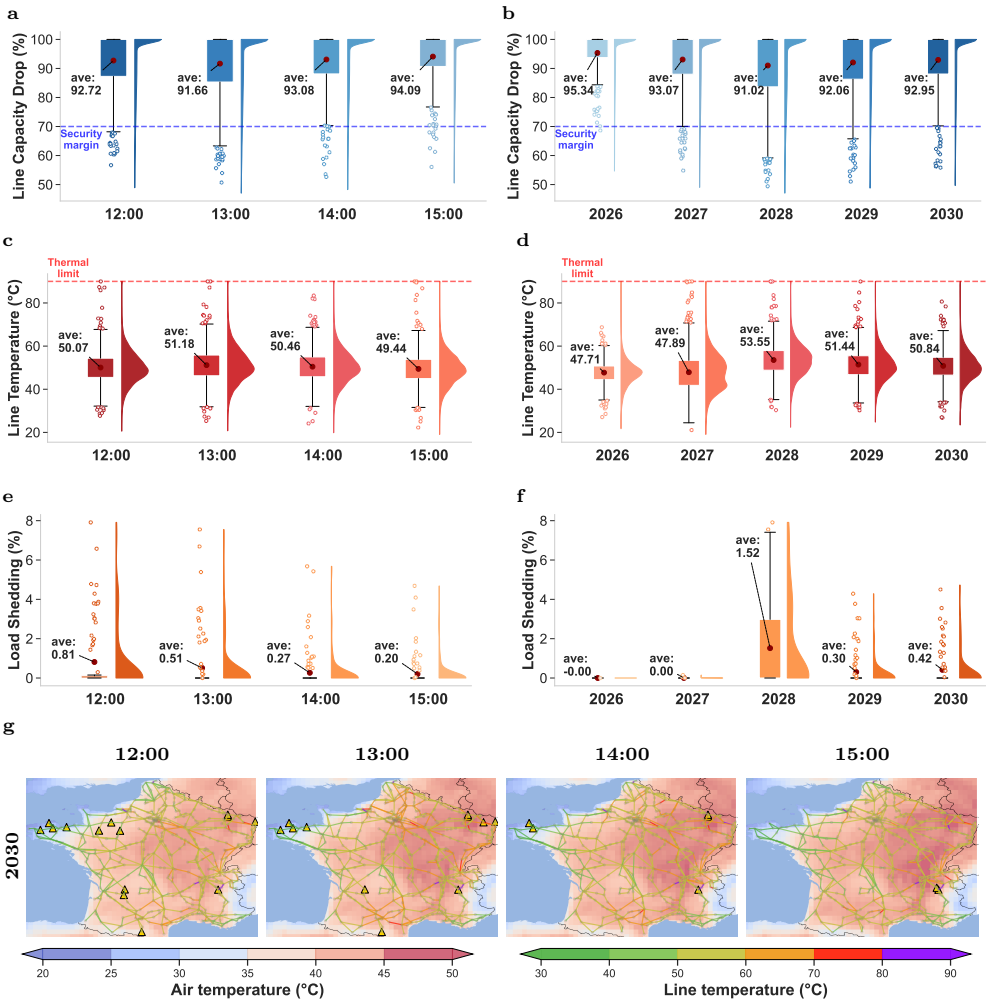

Supplementary Figure 22 | Spatiotemporal evolution of grid thermal stress and load shedding under heatwave conditions across diurnal and interannual scales. a–b Line capacity drop across different times of day (a) and projection years (b), with the security margin indicated by the dashed blue line. **c–d** Transmission line temperature variations across hours of day (c) and projection years (d); dashed red line indicates the thermal limit. **e–f** Load shedding ratios as a function of time of day (e) and projection year (f). **g** Power grid visualization showing the spatial distribution of air temperature (background shading; redder indicates higher temperature) and transmission line temperature (network overlay; red/purple indicates proximity to thermal limits) during peak afternoon hours (12:00–15:00) for a sampled heatwave scenario in 2030. Yellow triangles (△) indicate buses experiencing load shedding.

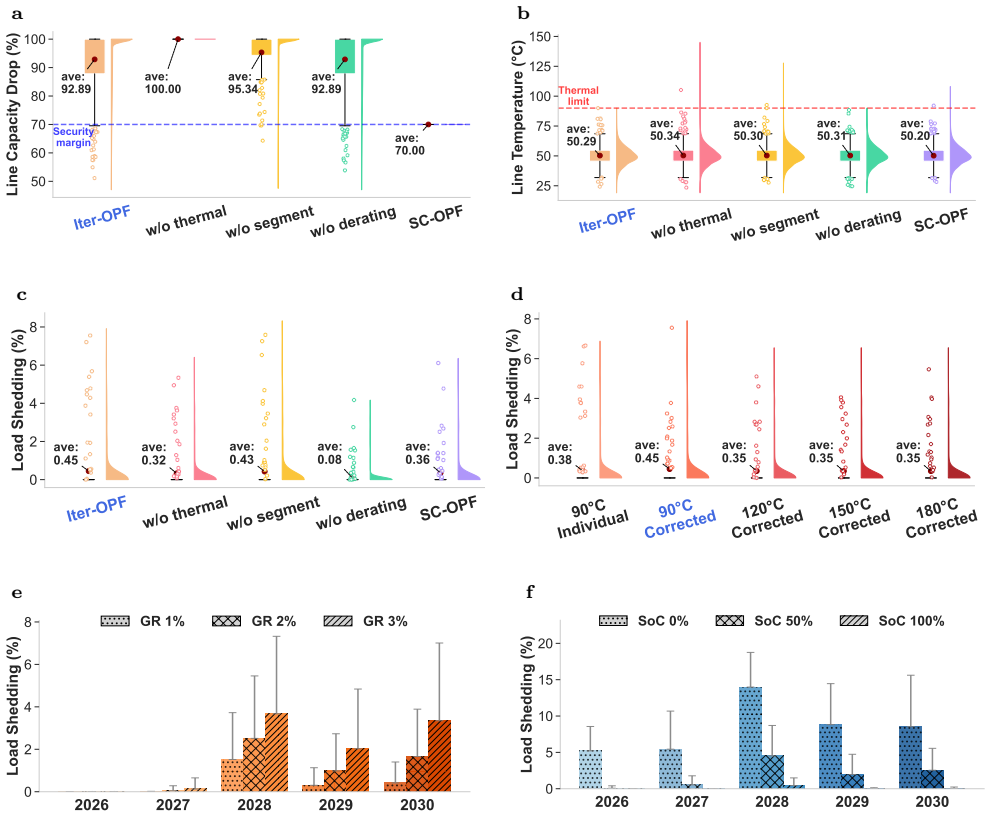

Supplementary Figure 23 | Diurnal-to-interannual evolution of grid performance and sensitivity to load growth and storage conditions under heatwave scenarios. f-h Impact of removing different modeling components from the Iter-OPF framework on capacity reduction (f), line temperatures (g), and load shedding ratios (h), compared to the 70% security margin SC-OPF method. **g–h** Sensitivity analysis of load shedding ratios under varying annual load growth rates (GR: 1%, 2%, and 3%) (g) and initial battery state-of-charge levels (SoC: 0%, 50%, and 100%) (h).

4.3 Cross-Border Analysis for Multiple Countries

We conduct **cross-border analysis** to examine grid interdependencies across multiple countries. We simulate reference countries both in isolation and jointly with neighbouring countries under identical heatwave scenarios, revealing how international interconnections influence key resilience metrics.

4.3.1 Spain and Neighboring Countries

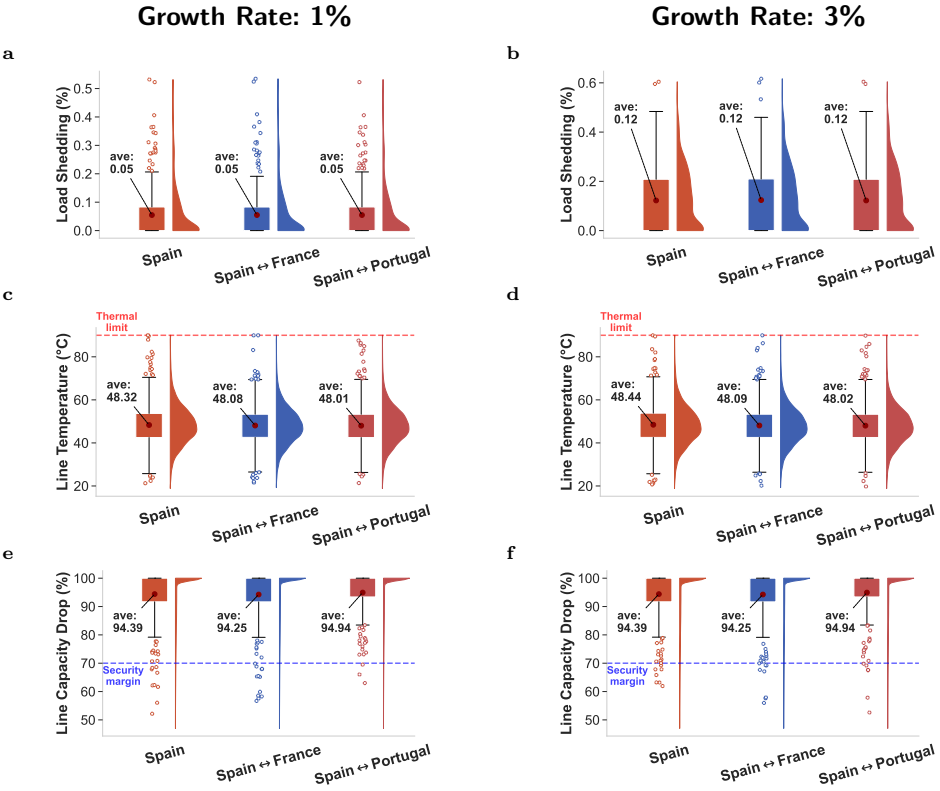

Supplementary Figure 24 | Cross-border interconnections impact grid resilience during heatwaves. We compare single-country analyses with joint multi-country analyses for the Spanish grid under identical heatwave projections to quantify the effects of cross-border interconnections on grid resilience. **a–b** Distribution of load shedding ratio in Spain across different interconnection scenarios under 1% (a) and 3% (b) annual load growth rates **c–d** Distribution of line temperature in Spain across different interconnection scenarios under 1% (c) and 3% (d) annual load growth rates. **e–f** Distribution of line capacity reduction in Spain across different interconnection scenarios under 1% (e) and 3% (f) annual load growth rates. Box plots display the median (centre line), interquartile range (box), and 1.5× interquartile range (whiskers); violin plots show the probability density distribution.

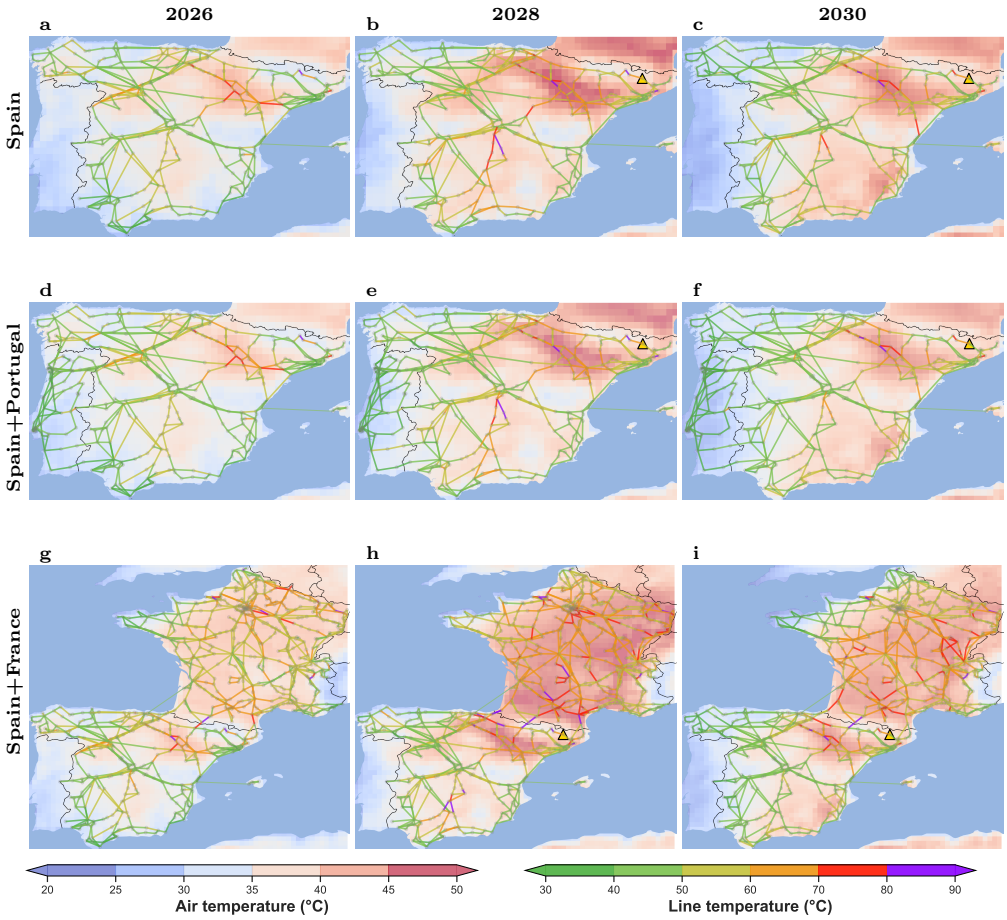

Supplementary Figure 25 | Cross-border Analysis for Spain, Portugal, and France in the baseline setting with load growth rate 1% and storage state 50%.

4.3.2 France and Neighboring Countries

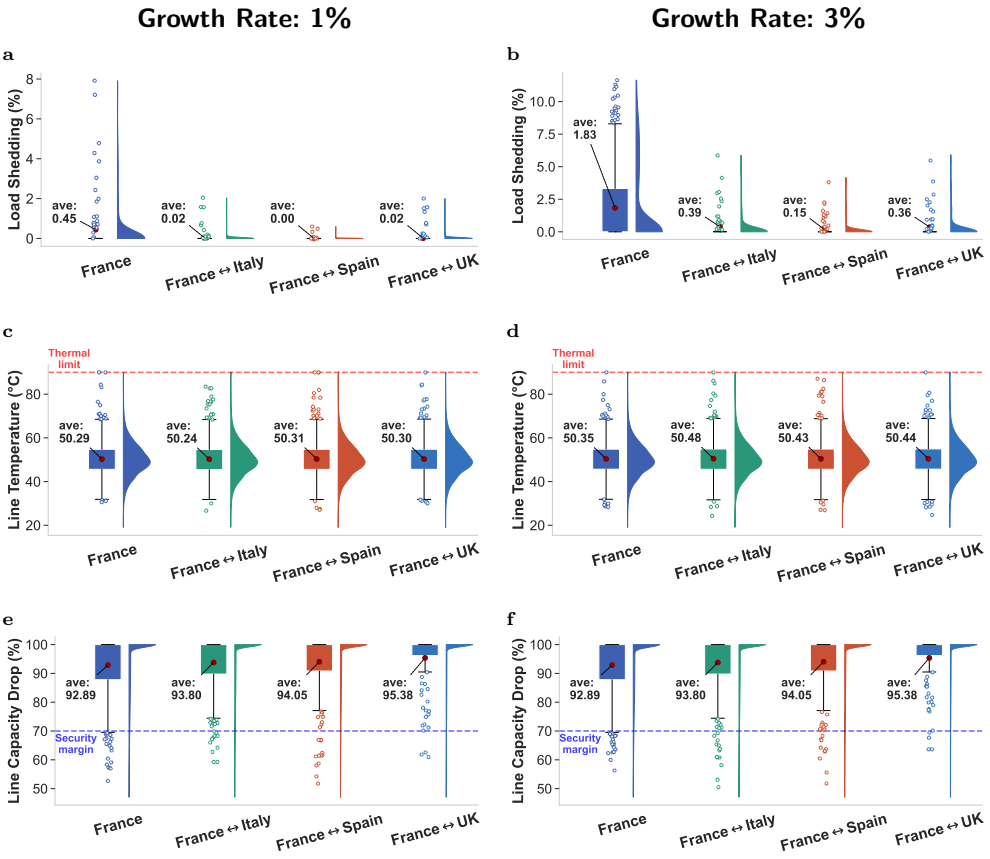

Supplementary Figure 26 | Cross-border interconnections impact grid resilience during heatwaves. We compare single-country analyses with joint multi-country analyses for the French grid under identical heatwave projections to quantify the effects of cross-border interconnections on grid resilience. **a–b** Distribution of load shedding ratio in France across different interconnection scenarios under 1% (a) and 3% (b) annual load growth rates **c–d** Distribution of line temperature in France across different interconnection scenarios under 1% (c) and 3% (d) annual load growth rates. **e–f** Distribution of line capacity reduction in France across different interconnection scenarios under 1% (e) and 3% (f) annual load growth rates. Box plots display the median (centre line), interquartile range (box), and 1.5× interquartile range (whiskers); violin plots show the probability density distribution.

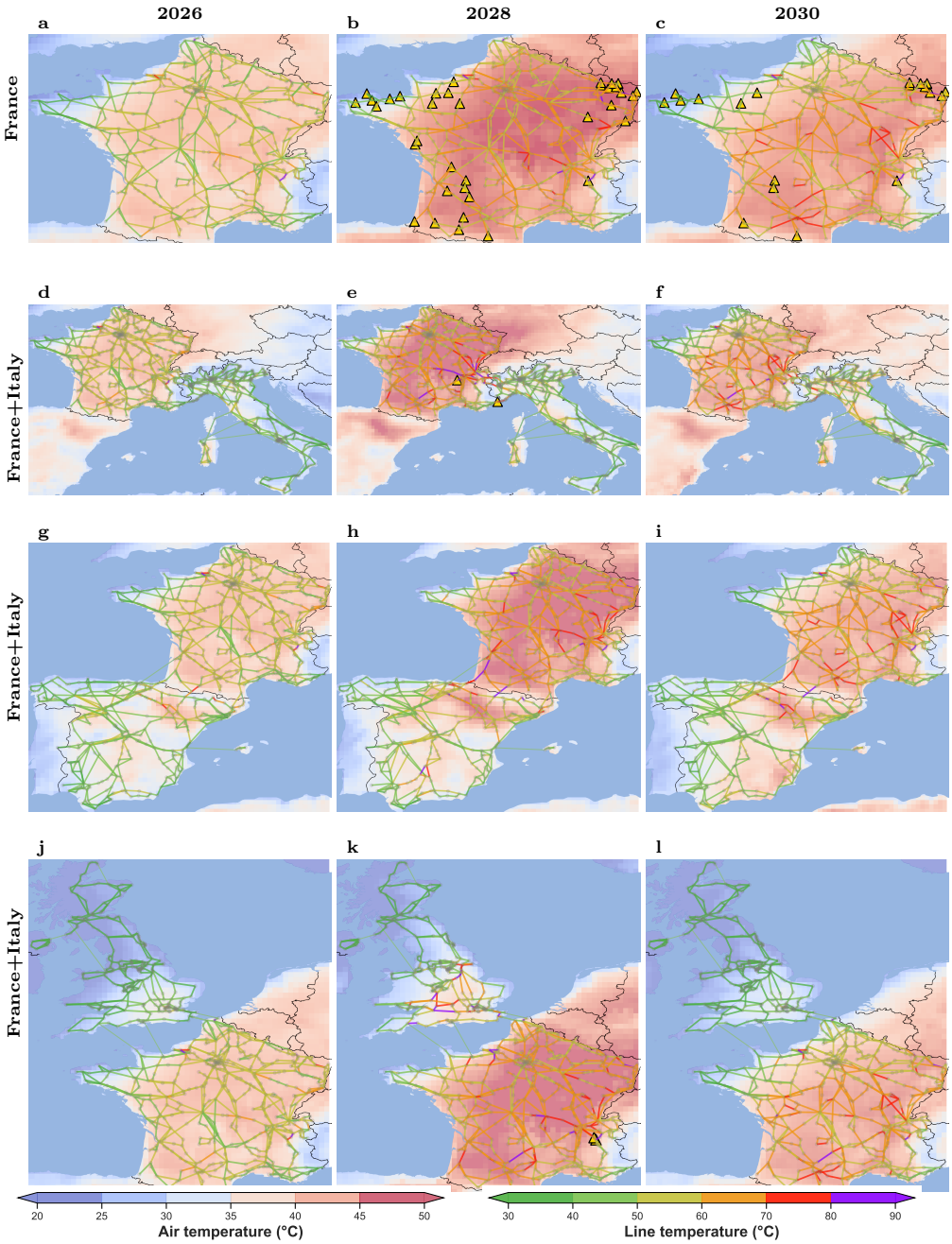

Supplementary Figure 27 | Cross-border Analysis for France, Italy, Spain, and UK in the baseline setting with load growth rate 1% and storage state 50%.

5 IEEE Benchmark Simulation

We use the IEEE 30-bus system as a benchmark to evaluate the effectiveness of our proposed methodology. This system comprises 30 nodes ($|\mathcal{N}| = 30$), 6 generators ($|\mathcal{G}| = 6$), 41 transmission lines ($|\mathcal{L}| = 41$), and 12 contingency scenarios ($|\mathcal{C}| = 12$). The number of contingency scenarios is fewer than the total number of transmission lines due to network connectivity constraints.

Our implementation adopts transmission line conductor specifications outlined in IEEE standards [33]. Security constraints are implemented using a preventive approach [34], in which real power generation dispatch at non-slack buses remains fixed across all post-contingency scenarios, while other control variables (such as reactive power and voltage magnitudes) may be adjusted in response to contingencies.

As shown in Table 10, we conduct a comparative analysis of multiple model formulations: the baseline model (AC-OPF), a temperature-dependent model with quadratic approximation of thermal constraints [35] (Quad-OPF), our proposed iterative approach (Iter-OPF), and the fully converged temperature-dependent OPF solution (TD-OPF). We also evaluate ablated variants of the iterative approach (Iter-OPF), excluding either thermal modeling (w/o thermal) or derating modeling (w/o derating). Additionally, we compare our thermal-based modeling approach against security-constrained AC-OPF formulations (detailed in Sec. 2.2), including AC-SC-OPF, the complete $N-1$ AC-based security-constrained formulation; DC-SC-OPF, AC-OPF with security margins approximated via line outage distribution factors; and fixed-SC-OPF, AC-OPF with a fixed 70% security margin.

We note that several studies employ DC-OPF-based formulations incorporating weather-dependent dynamic line rating approaches [18]. However, these DC models are not AC-feasible due to their linear simplifications and fail to capture the coupling effects between power flow and heat transfer. Accordingly, we consider only AC-based models in our evaluation.

Supplementary Table 10 | Model Baselines for the IEEE-30 Simulations.

Models	**Conductor model** Thermal	**Generator** Derating	**Contingency** Security Constraint
	Models Baselines		
AC-OPF	✗	✗	✗
Quad-OPF	quad. approx.	✗	✗
Iter-OPF	✓	✓	✓
TD-OPF	✓	✓	✓
	Sensitivity Analysis		
w/o thermal	✗	✓	✓
w/o derating	✓	✗	✓
AC-SC-OPF	✗	✗	Exact
DC-SC-OPF	✗	✗	Linear
Fix-SC-OPF	✗	✗	Fixed

5.1 Thermal Modeling is Essential for Grid Resilience Assessment

We first compare model performance under a load ratio of 0.9 relative to the default IEEE case across different weather profiles (Fig. 28), including mild weather conditions (wind speed of 0.61 m/s and ambient temperature of 25°C) [33] and extreme weather conditions (wind speed of 0.1 m/s and ambient temperature of 45°C).

Under mild weather conditions, the baseline AC-OPF, Quad-OPF, Iter-OPF, and TD-OPF all achieve zero load shedding while maintaining thermal feasibility. However, under extreme weather conditions, the thermal-aware models (Iter-OPF and TD-OPF) appropriately increase load shedding to 8.06%, accurately reflecting the reduced line ampacity at elevated ambient temperatures. In contrast, the baseline AC-OPF maintains zero load shedding but produces widespread thermal violations, with line temperatures exceeding the 90°C safety threshold. The Quad-OPF formulation exhibits lower load shedding due to its quadratic approximation of thermal constraints, which permits slight temperature exceedances under extreme conditions—a potentially unsafe operating regime.

Ablation studies confirm the necessity of both modelling components. Removing thermal modelling leads to systematically underestimated line temperatures and undetected thermal violations. Removing derating modelling results in 7.09% load shedding under extreme conditions, demonstrating that accurate capacity derating is essential for reliable dispatch. Notably, Iter-OPF achieves solution quality comparable to the fully converged TD-OPF while requiring substantially less computational time (0.42 s versus 1.03 s), demonstrating the efficiency of our iterative scheme.

5.2 Security Constraints Cause Excessive Curtailment Under Normal Conditions and Insufficient Protection Under Stress

Security-constrained formulations (shown in Fig. 28), by contrast, exhibit weather-independent behaviour. AC-SC-OPF requires 7.29% load shedding with the highest computational cost (2.07 s); DC-SC-OPF requires 6.33% with moderate cost (0.83 s); and Fixed-SC-OPF requires 4.18% using a conservative 70% security margin. These static approaches impose fixed margins regardless of ambient conditions, incurring unnecessary load shedding even under mild weather while still permitting line temperatures to exceed 90°C during extreme events. This dual failure mode—excessive curtailment under normal conditions and insufficient protection under stress—highlights the fundamental limitation of weather-agnostic security margins.

Our thermal-aware formulation addresses this limitation by dynamically adjusting line capacity based on real-time electrothermal interactions. This adaptive behaviour maximises transmission asset utilisation during favourable conditions while ensuring adequate protection during thermal stress events.

These findings underscore the importance of comprehensive electrothermal modelling that captures the complex interactions among weather conditions, transmission line capabilities, and generation dispatch during extreme events. As climate change

increases the frequency and severity of such events, physics-based thermal modelling becomes increasingly critical for ensuring grid resilience.

5.3 Compound Effects of Extreme Weather: High-Temperature and Low-Wind

We further examine model performance under four weather scenarios—mild (0.61 m/s, 25°C), low-wind (0.1 m/s, 25°C), high-temperature (0.61 m/s, 45°C), and extreme (0.1 m/s, 45°C)—across two load ratios (0.9 and 1.0) to assess the compound effects of adverse weather conditions (Fig. 29).

At the 0.9 load ratio compared to the default load, AC-OPF achieves zero load shedding across all weather scenarios but produces thermal violations under high-temperature and extreme conditions (Fig. 29b). Iter-OPF maintains zero load shedding under mild, low-wind, and high-temperature conditions, and reaches 8.06% under extreme weather—appropriately reflecting the compounding effect of reduced convective cooling (low wind) and elevated ambient temperature on line ampacity. Security-constrained formulations require constant load shedding (7.29% for AC-SC-OPF; 4.18% for Fixed-SC-OPF) regardless of weather conditions.

At the 1.0 load ratio, these patterns intensify (Fig. 29c,d). AC-OPF continues to show zero load shedding but with more severe thermal violations exceeding 120°C. Iter-OPF exhibits weather-responsive behaviour: zero load shedding under mild conditions, 0.69% under low-wind, 4.12% under high-temperature, and 16.48% under extreme weather. This progressive increase demonstrates the model's ability to capture the nonlinear interaction between weather stressors. Security-constrained approaches again show weather-invariant curtailment (16.39% for AC-SC-OPF; 12.85% for Fixed-SC-OPF), over-curtailing under mild conditions while providing no additional margin under thermal stress.

These results reveal that extreme weather events produce compound effects that static security margins cannot adequately address. Our thermal-aware formulation captures the physics of electrothermal coupling, enabling weather-adaptive dispatch that maximises grid efficiency under favourable conditions while ensuring safe operation during compound stress events.

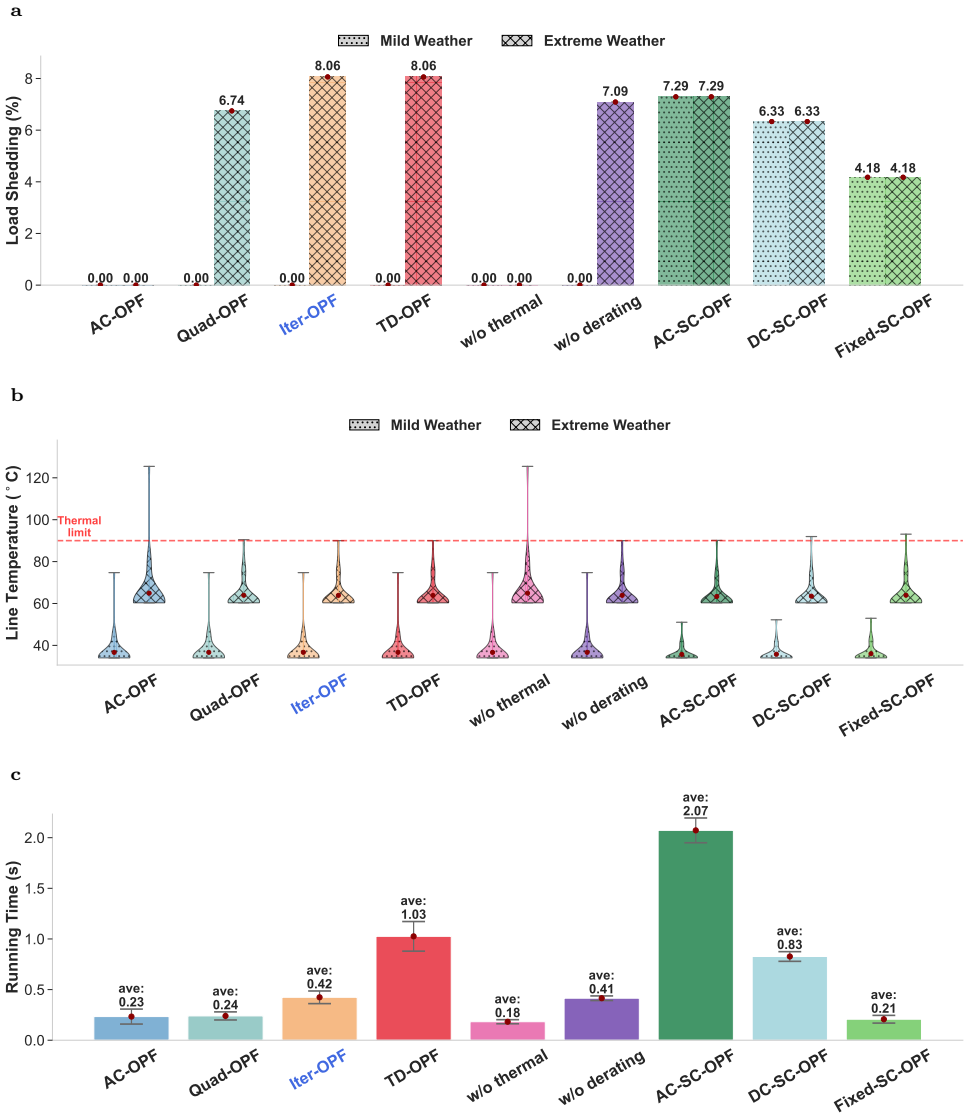

Supplementary Figure 28 | Thermal analysis results for the IEEE 30-bus system under different load and weather conditions. **a** Load shedding percentage across model formulations under mild and extreme weather conditions. **b** Distribution of line temperatures across all transmission lines; the red dashed line indicates the thermal limit (90°C). **c** Computational running time for each formulation. Error bars represent standard deviation across test instances.

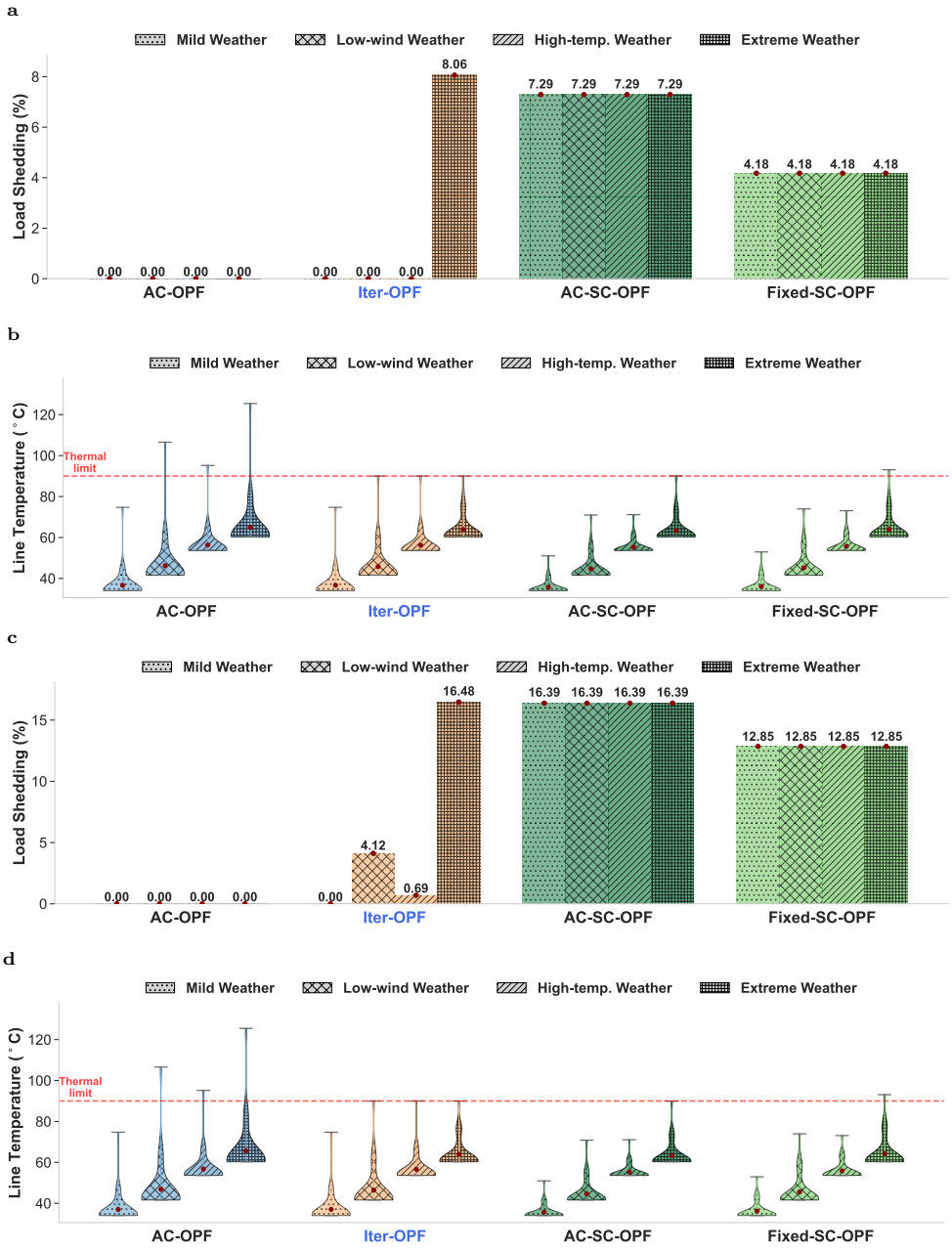

Supplementary Figure 29 | Sensitivity analysis results for the IEEE 30-bus system under different load and weather conditions. **a-b** Load shedding percentage and line temperature distribution at 0.9 load ratio. **c-d** Load shedding percentage and line temperature distribution at 1.0 load ratio. The red dashed line indicates the thermal limit (90°C).

References

[1] Hörsch, J., Hofmann, F., Schlachtberger, D. & Brown, T. Pypsa-eur: An open optimisation model of the european transmission system. *Energy strategy reviews* **22**, 207–215 (2018).

[2] Hersbach, H. *et al.* The era5 global reanalysis. *Quarterly journal of the royal meteorological society* **146**, 1999–2049 (2020).

[3] Copernicus Climate Change Service. Climate and energy indicators for europe from 2005 to 2100 derived from climate projections (2021). URL https://cds.climate.copernicus.eu/datasets/sis-energy-derived-projections?tab=overview. Accessed: 2024-10-06.

[4] Hirth, L., Mühlenpfordt, J. & Bulkeley, M. The entso-e transparency platform–a review of europe's most ambitious electricity data platform. *Applied energy* **225**, 1054–1067 (2018).

[5] Staffell, I., Pfenninger, S. & Johnson, N. A global model of hourly space heating and cooling demand at multiple spatial scales. *Nature Energy* 1–17 (2023).

[6] Hofmann, F., Hampp, J., Neumann, F., Brown, T. & Hörsch, J. Atlite: a lightweight python package for calculating renewable power potentials and time series. *Journal of Open Source Software* **6**, 3294 (2021).

[7] Cain, M. B., O'neill, R. P., Castillo, A. *et al.* History of optimal power flow and formulations. *Federal Energy Regulatory Commission* **1**, 1–36 (2012).

[8] Tang, Y., Dvijotham, K. & Low, S. Real-time optimal power flow. *IEEE Transactions on Smart Grid* **8**, 2963–2973 (2017).

[9] Jabr, R. A., Karaki, S. & Korbane, J. A. Robust multi-period opf with storage and renewables. *IEEE Transactions on Power Systems* **30**, 2790–2799 (2014).

[10] Capitanescu, F. *et al.* State-of-the-art, challenges, and future trends in security constrained optimal power flow. *Electric power systems research* **81**, 1731–1741 (2011).

[11] Brown, T., Hörsch, J. & Schlachtberger, D. Pypsa: Python for power system analysis. *arXiv preprint arXiv:1707.09913* (2017).

[12] Hörsch, J., Ronellenfitsch, H., Witthaut, D. & Brown, T. Linear optimal power flow using cycle flows. *Electric Power Systems Research* **158**, 126–135 (2018).

[13] Frank, S., Sexauer, J. & Mohagheghi, S. Temperature-dependent power flow. *IEEE Transactions on Power Systems* **28**, 4007–4018 (2013).

[14] Ahmed, A., McFadden, F. J. S. & Rayudu, R. Weather-dependent power flow algorithm for accurate power system analysis under variable weather conditions. *IEEE Transactions on power systems* **34**, 2719–2729 (2019).

[15] Neumann, F., Hagenmeyer, V. & Brown, T. Assessments of linear power flow and transmission loss approximations in coordinated capacity expansion problems. *Applied Energy* **314**, 118859 (2022).

[16] Glaum, P. & Hofmann, F. Leveraging the existing german transmission grid with dynamic line rating. *Applied Energy* **343**, 121199 (2023).

[17] Abboud, A. W., Gentle, J. P., Parikh, K. & Coffey, J. Sensitivity effects of high temperature overhead conductors to line rating variables. Tech. Rep., Idaho National Lab.(INL), Idaho Falls, ID (United States) (2020).

[18] Karimi, S., Musilek, P. & Knight, A. M. Dynamic thermal rating of transmission lines: A review. *Renewable and Sustainable Energy Reviews* **91**, 600–612 (2018).

[19] Manninen, H., Lippus, M. & Rute, G. Dynamic line rating using hyper-local weather predictions: A machine learning approach. *arXiv preprint arXiv:2405.12319* (2024).

[20] Ngoko, B. O., Sugihara, H. & Funaki, T. Optimal power flow considering line-conductor temperature limits under high penetration of intermittent renewable energy sources. *International Journal of Electrical Power & Energy Systems* **101**, 255–267 (2018).

[21] Hörsch, J. & Brown, T. *The role of spatial scale in joint optimisations of generation and transmission for european highly renewable scenarios*, 1–7 (IEEE, 2017).

[22] Neumann, F. & Brown, T. *Heuristics for transmission expansion planning in low-carbon energy system models*, 1–8 (IEEE, 2019).

[23] Nigol, O. & Barrett, J. Characteristics of acsr conductors at high temperatures and stresses. *IEEE Transactions on Power Apparatus and Systems* 485–493 (1981).

[24] Douglass, D. & Reding, J. Ieee standard for calculating the current-temperature of bare overhead conductors. *IEEE Standard* 738–2006 (2007).

[25] ENTSO-E. Technologies for transmission system. Technical Report, European Network of Transmission System Operators for Electricity (2018). URL https://eepublicdownloads.blob.core.windows.net/public-cdn-container/clean-documents/tyndp-documents/TYNDP2018/consultation/Technical/Technologies4TS.pdf. TYNDP 2018.

[26] Brown, T., Schierhorn, P.-P., Tröster, E. & Ackermann, T. Optimising the european transmission system for 77% renewable electricity by 2030. *IET Renewable Power Generation* **10**, 3–9 (2016).

[27] Duan, Q. *et al.* Pypop7: A pure-python library for population-based black-box optimization. *Journal of Machine Learning Research* **25**, 1–28 (2024).

[28] Ieee standard for calculating the current-temperature relationship of bare overhead conductors. *IEEE Std 738-2012 (Revision of IEEE Std 738-2006 - Incorporates IEEE Std 738-2012 Cor 1-2013)* 1–72 (2013).

[29] Kanálik, M., Margitová, A., Urbanskỳ, J. & Beňa, L. *Temperature calculation of overhead power line conductors according to the cigre technical brochure 207*, 1–5 (IEEE, 2019).

[30] ENTSO-E. High temperature low sag conductors (htls). Technopedia. URL https://www.entsoe.eu/Technopedia/techsheets/high-temperature-low-sag-conductors-htls. Technical Sheet.

[31] Yang, W. *et al.* Thermal analysis for multi-conductor bundle in high voltage overhead transmission lines under the effect of strong wind. *Electric Power Systems Research* **231**, 110308 (2024).

[32] Ngoko, B., Sugihara, H. & Funaki, T. *A temperature dependent power flow model considering overhead transmission line conductor thermal inertia characteristics*, 1–6 (IEEE, 2019).

[33] Muratori, B. Ieee standard for calculating the current-temperature relationship of bare overhead conductors. *IEEE Standard* 738–2012 (2013).

[34] Capitanescu, F., Glavic, M., Ernst, D. & Wehenkel, L. Contingency filtering techniques for preventive security-constrained optimal power flow. *IEEE Transactions on Power Systems* **22**, 1690–1697 (2007).

[35] Ahmed, A., Massier, T., McFadden, F. S. & Rayudu, R. *Weather-dependent ac power flow algorithms*, 1–8 (IEEE, 2020).